1-15-2019

Effects of ball milling on the structure of cotton cellulose

Zhe Ling
Beijing Forestry University

Tuo Wang
Louisiana State University

Mohamadamin Makarem
Pennsylvania State University

Michael Santiago Cintrón
USDA ARS Southern Regional Research Center

H. N. Cheng
USDA ARS Southern Regional Research Center

See next page for additional authors

Recommended Citation

Ling, Z., Wang, T., Makarem, M., Santiago Cintrón, M., Cheng, H., Kang, X., Bacher, M., Potthast, A., Rosenau, T., King, H., Delhom, C., Nam, S., Vincent Edwards, J., Kim, S., Xu, F., & French, A. (2019). Effects of ball milling on the structure of cotton cellulose. *Cellulose, 26* (1), 305-328. https://doi.org/10.1007/s10570-018-02230-x

Cellulose

Effects of ball milling on the structure of cotton cellulose

--Manuscript Draft--

Manuscript Number:	
Full Title:	Effects of ball milling on the structure of cotton cellulose
Article Type:	S.I. : Cellulose 25th Anniversary
Keywords:	Amorphous cellulose; Ball milling; Cellulose Degradation; Crystal structure; Rietveld refinement
Corresponding Author:	Alfred D. French, Ph.D. USDA - United States Dept. Of Agriculture New Orleans, LA UNITED STATES
Corresponding Author Secondary Information:	
Corresponding Author's Institution:	USDA - United States Dept. Of Agriculture
Corresponding Author's Secondary Institution:	
First Author:	Zhe Ling
First Author Secondary Information:	
Order of Authors:	Zhe Ling
	Tuo Wang
	Mohamadamin Makarem
	Michael Santiago Cintrón
	H.N. Cheng
	Xue Kang
	Markus Bacher
	Antje Potthast
	Thomas Rosenau
	Holly King
	Christopher D. Delhom
	Sunghyun Nam
	J. Vincent Edwards
	Seong H. Kim
	Feng Xu
	Alfred D. French, Ph.D.
Order of Authors Secondary Information:	
Funding Information:	Chinese Scholarship Council (CSC No.201706510045) — Mr. Zhe Ling
	National Science Foundation (NSF OIA-1833040) — Professor Tuo Wang
	US Department of Energy (DE-SC0001090) — Prof. Seong H. Kim
Abstract:	Cellulose is often described as a mixture of crystalline and amorphous material. A large part of the general understanding of the chemical, biochemical and physical properties of cellulosic materials is thought to depend on the consequences of the ratio of these

	components. For example, amorphous materials are said to be more reactive and have less tensile strength but comprehensive understanding and definitive analysis remain elusive. Ball milling has been used for decades to increase the ratio of amorphous material. The present work used 13 techniques to follow the changes in cotton fibers (nearly pure cellulose) after ball milling for 15, 45 and 120 minutes. X-ray diffraction results were analyzed with the Rietveld method; DNP (Dynamic Nuclear Polarization) natural abundance 2-D NMR studies in the following paper assisted with the interpretation of the 1-D analyses in the present work. A conventional NMR model's paracrystalline and inaccessible crystallite surfaces were not needed in the model used for the DNP studies. Sum Frequency Generation spectroscopy also showed profound changes as the cellulose was decrystallized. Optical microscopy and FE-SEM results showed the changes in particle size; molecular weight and carbonyl group analyses by gel permeation chromatography (GPC) confirmed chemical changes. Specific surface areas and pore sizes increased. Fourier Transform IR and Raman spectroscopy also indicated progressive changes; some proposed indicators of crystallinity for FTIR were not in good agreement with our results. Thermogravimetric analysis results indicated progressive increase in initial moisture content and some loss in stability.
Suggested Reviewers:	Tom Elder USDA Forest Service Pacific Southwest Region telder@fs.fed.us generally knowledgeable on cellulose structure
	Umesh Agarwal USDA Forest Service Forest Products Lab Madison uagarwal@fs.fed.us Has published in this area
	Steve Eichhorn University of Bristol s.j.eichhorn@bristol.ac.uk Experienced in many relevant aspects of this work

Dear Handling Editor,

The manuscript “Effects of ball milling on the structure of cotton cellulose” describes the changes in various properties of cotton cellulose during ball milling. The headline methods are Rietveld analysis of both laboratory and synchrotron X-ray diffraction, ssNMR informed by the accompanying paper on 2D natural abundance NMR on two of the same samples, and Sum Frequency Generation spectroscopy, which, to my knowledge, have not been applied to ball-milled cotton. Supporting methods include a more conventional ^{13}C NMR analysis, FTIR and Raman spectroscopy, optical microscopy, Field Emission Scanning Electron Microscopy, molecular weight analysis and carbonyl and uronic acid group determination.

This effort on a classic problem (ball-milled cotton crystallinity research has been done for nearly 70 years) was conceived as particularly suited to the 25Th Anniversary issue. A goal was to get the diffraction and spectroscopy scientists to try to resolve the differences in understanding of the results. There are some novel results, such as the finding by all three headline methods that some crystalline cellulose I remains after two hours of ball milling. The X-ray analyses on data from two different approaches agreed that not only did the fraction of crystalline material decrease, but so did the size of the remaining crystallites. The understanding of the domain sizes for the Ialpha, and Ibeta signals in NMR and the parallel chain domains in SFG studies seem to need a revision in understanding.

The manuscript CELS-D-18-00951_2D_DNP.pdf is attached as supplementary material, as is the X-ray data in Excel format. There is a main Supplementary Material .pdf file that includes extra figures and tables for the manuscript. The other manuscript is for the use of the reviewers if needed to review the ssNMR work in the present manuscript. These two manuscripts are intended for adjacent publication, with this one serving to introduce the already submitted one.

The USDA has a manuscript approval process that requires pre-submission review. Reviewers included Dr. Hee Jin Kim of the USDA SRRC, HeeJin.Kim@ars.usda.gov

and

Dr. Stephanie Beck, FPInnovations: Stephanie.beck@fpinnovations.ca

Suggested reviewers include stalwarts such as

Umesh Agarwal, uagarwal@fs.fed.us

Tom Elder, telder@fs.fed.us

Steve Eichhorn, s.j.eichhorn@bristol.ac.uk

Best wishes.

Al French

Effects of ball milling on the structure of cotton cellulose

Zhe Ling · Tuo Wang · Mohamadamin Makarem · Michael Santiago Cintrón · H. N. Cheng · Xue Kang · Markus Bacher · Antje Potthast · Thomas Rosenau, Holly King · Christopher D. Delhom · Sunghyun Nam · J. Vincent Edwards · Seong H. Kim ·, Feng Xu · Alfred D. French*

Zhe Ling · Feng Xu, Beijing Key Laboratory of Lignocellulosic Chemistry, Beijing Forestry University, Beijing 100083, PR China

Zhe Ling · Michael Santiago Cintrón · H. N. Cheng · Holly King · Christopher D. Delhom · Sunghyun Nam · J. Vincent Edwards · Alfred D. French* · Southern Regional Research Center, Agricultural Research Service, USDA, 1100 Robert E. Lee Blvd., New Orleans, LA 70124, USA

Xue Kang, Tuo Wang Department of Chemistry, Louisiana State University, Baton Rouge, LA 70803, USA

Mohamadamin Makarem · Seong H. Kim Department of Chemical Engineering and Material Research Institute, The Pennsylvania State University, University Park, PA 16802, USA

Thomas Rosenau, Markus Bacher, Antje Potthast Department of Chemistry, Division of Chemistry of Renewable Resources, University of Natural Resources and Life Sciences, Konrad-Lorenz-Str. 24, A-3430 Tulln, Austria

Corresponding author:

Alfred D. French

Email: al.french@ars.usda.gov, Tel: 1-5042864410

ORCID: 0000-0002-6220-6448

Prepared for Cellulose 25th Anniversary Special Issue

Version of 10/13/2018

Abstract Cellulose is often described as a mixture of crystalline and amorphous material. A large part of the general understanding of the chemical, biochemical and physical properties of cellulosic materials is thought to depend on the consequences of the ratio of these components. For example, amorphous materials are said to be more reactive and have less tensile strength but comprehensive understanding and definitive analysis remain elusive. Ball milling has been used for decades to increase the ratio of amorphous material. The present work used 13 techniques to follow the changes in cotton fibers (nearly pure cellulose) after ball milling for 15, 45 and 120 minutes. X-ray diffraction results were analyzed with the Rietveld method; DNP (Dynamic Nuclear Polarization) natural abundance 2-D NMR studies in the following paper assisted with the interpretation of the 1-D analyses in the present work. A conventional NMR model's paracrystalline and inaccessible crystallite surfaces were not needed in the model used for the DNP studies. Sum Frequency Generation spectroscopy also showed profound changes as the cellulose was decrystallized. Optical microscopy and FE-SEM results showed the changes in particle size; molecular weight and carbonyl group analyses by gel permeation chromatography (GPC) confirmed chemical changes. Specific surface areas and pore sizes increased. Fourier Transform IR and Raman spectroscopy also indicated progressive changes; some proposed indicators of crystallinity for FTIR

were not in good agreement with our results. Thermogravimetric analysis results indicated progressive increase in initial moisture content and some loss in stability.
Keywords Amorphous cellulose · Ball milling · Cellulose Degradation · Crystal structure · Rietveld refinement

Introduction

Cellulose is often described as a two-phase material, with both crystalline and amorphous domains. It is widely thought that crystalline materials are stronger and less-reactive than their amorphous counterparts. Therefore, it has been of interest for nearly a century to understand these two components to better develop structure-function relationships for both natural and modified cellulosic materials.

The idea that cellulose has a crystalline component came from X-ray diffraction. According to the International Union of Crystallographers, any material (including cotton cellulose) that yields a diffraction pattern with sharp peaks is crystalline. Nishiyama et al. (2003a, 2002) published crystal structures of the Iα and Iβ native celluloses from the alga *Cladophora* and tunicate with atomic coordinates, based on both neutron and synchrotron X-ray studies.

The idea that everyday plant cellulose is not entirely crystalline came from several directions. In the case of diffraction, the peaks are not as sharp as those from many smaller molecules. That increase in peak breadth could come from

small crystallite size, from defects within the crystal lattice, or from material that lacks organization, causing the crystalline peaks to be more diffuse (Wertz et al. 2010). Concepts of synthetic petrochemical polymers gave us the "fringed micelle" model and its nuanced "fringed fibril" variant (Hearle 1958) that has individual, long molecules passing through numerous domains of local organization. In between these local domains, or crystallites, the molecules lacked sufficient organization to diffract X-rays into sharp peaks. Another insight from diffraction is that the amorphous regions in ramie cellulose are quite small (Nishiyama et al. 2003b) and distances between the regions are comparable to molecular lengths from Leveling Off Degree of Polymerization (LODP) studies.

Isogai and Atalla (1991) regenerated samples by precipitating cellulose from SO_2-diethylamine-dimethylsulfoxide solutions with various precipitants. Unlike other regenerated celluloses, their precipitates were amorphous, and the exact X-ray scattering patterns differed, depending on the particular precipitating anti-solvent. Vibrational spectroscopists identified a group of low frequency vibrations that were necessary conditions for crystallinity (Agarwal et al. 2016). Those vibrations were absent in some native cellulose samples that still give diffraction patterns that the authors interpreted as indications of an aligned but non-crystalline state. These observations indicate that there are nuances to non-crystalline states and models for the disordered components must incorporate flexibility.

Cotton fibers are individual plant cells, and their cell walls, which consist mostly of cellulose, have additional structural features of interest. In particular, the crystallites of native cellulose are composed of molecules with their reducing groups at one end of the crystal, described as parallel packing. Since the crystallites are generally aligned with the fiber axis[1] one might describe the crystallite as oriented with the reducing end of the crystal towards the growth tip of the cotton fiber. Based in part on findings that the molecules in crystals of mercerized cellulose II are packed antiparallel, however, it has been concluded that adjacent to the crystallites "pointed" towards the fiber growth tip, there is another set of cotton crystallites oriented in the opposite direction. This finding was supported by sum frequency generation (SFG) spectroscopic studies (Lee et al. 2014). These oppositely oriented crystallites, each with parallel-packed molecules, can, after swelling with NaOH, merge to create crystals with their molecules packed antiparallel while retaining the overall fiber structure (Sarko et al. 1987; Shibazaki et al. 1997; French et al., 2018).

An early experiment with ball milling reduced the cotton sample to the amorphous state in 30 min (our ball milling system is slower) (Forziati et al. 1950). Subsequently, Segal et al. (1959) developed a crystallinity index (Fig. 1) to

[1] Even though cotton has a high microfibril angle (French and Kim 2018) or range of deviations of alignment of microfibrils to the fiber axis, for this discussion the alignment of adjacent microfibrils can be considered to be antiparallel.

indicate the fraction of crystalline material in the sample. That publication has been cited some 3,650 times at this writing, and their equation is often used without proper credit.[2] In that paper, the Segal crystallinity index (CrI) was compared with acid crystallinity, LODP, density, moisture regain, and an infrared crystallinity

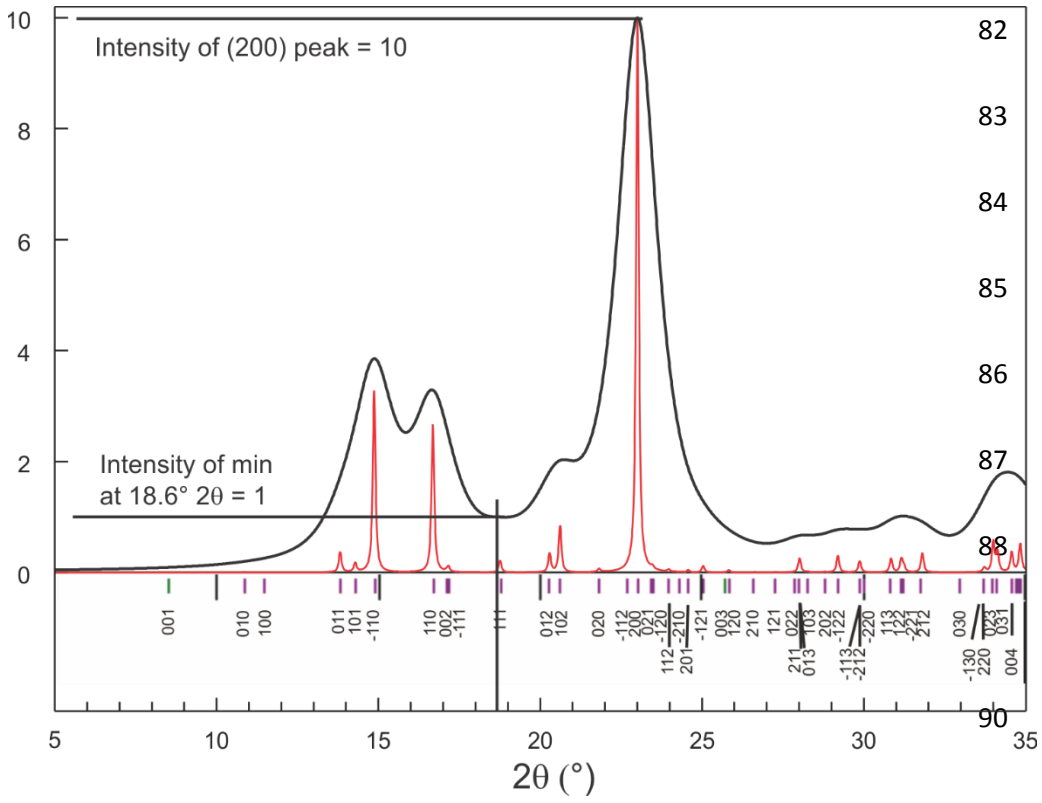

Fig. 1 Calculated diffraction patterns for peak widths at half height (pwhm) of 0.1 (red) and 1.5° (black), based on the crystal structure of cellulose Iβ (Nishiyama et al. 2002). The corresponding Miller indices are plotted for each possible peak,

[2] Despite its simplicity, the Segal method is sometimes used incorrectly. The Segal CrI depends on the intensity minimum between the (110) and (200) peaks, as well as the peak intensity of the (200) reflection. However, authors have too-often chosen the (110) or combined (1-10) and (110) peak as representing the amorphous material. Furthermore, for material to be represented by the minimum intensity near 18 deg. (copper Kα radiation), the background must be subtracted. Typically, this would mean subtraction of a blank.

indicated by the vertical magenta lines. The values of 2θ are for a wavelength of 1.5419 Å (CuKα). The Segal CrI is $CrI = 100 * (I_{200} - I_{am})/I_{200}$, where I_{200} is the height of the (200) peak, and I_{am} is the intensity at the minimum at about 18.6° 2θ. Both calculations are based on perfect crystal models, but with sizes of about 900 Å (when pwhm = 0.1°) and 60 Å (pwhm = 1.5°). In this case the smaller crystallite would have a CrI of 90 %, whereas the larger one would have a CrI of 100%. Adapted from Fig. 2a in French (2014)

index. In the intervening years, researchers have attempted to confirm the Segal equation with numerous methods including infrared spectroscopy (Nelson and O'Connor 1964a) and deuterium exchange (Agarwal 2016).

Many such tests could confuse the increase of specific surface area with a decrease in the crystallinity, even though the smaller crystals with more surface area might be perfectly ordered. Another point is that surface molecules become an increasingly large fraction of the total molecules as the crystals are reduced in size. A crystal with 100 molecules (a more or less square shape with 10 molecules on each side) will have 36 molecules (36%) on the surface that are not as constrained by neighbors within the crystal. A similarly shaped crystal with only 36 molecules would have 20 molecules on the surface, or 55%. The O-6 groups on surface molecules would have extra freedom for rotation and occupation of the alternative

115 *gauche-trans* (*gt*) and *gauche-gauche* (*gg*) positions. The O-6 positions will affect
116 various key spectroscopic results more than they would X-ray diffraction
117 intensities. An O-6 in the *gt* position has very similar x- and y- coordinates as one
118 in the usual *trans-gauche* (*tg*) cellulose I position and the very strong hk0
119 diffraction intensities would not be affected very much. Because different
120 crystallinity techniques measure different things, complete agreement among
121 different methods may never be attained.

122 Segal's landmark equation was criticized, especially because the area under
123 the peaks is more important than their height. More recently, French and Santiago
124 Cintrón (2013) showed that some of the diffraction intensity attributed to
125 amorphous material by Segal et al. can be due to the overlap of the broad peaks
126 resulting from small crystallites, as in Fig. 1. Also, there is a small contribution to
127 Segal's amorphous intensity from some small peaks. Therefore, no cellulose
128 sample with reasonable crystallite size could give 100 % Segal crystallinity. A
129 further deficit in Segal's approach is that a sample that was 100% amorphous
130 would have to give a diffraction pattern with a flat top. Instead, amorphous
131 samples, regardless of source, give a broad hump with a maximum that reflects the
132 distribution of frequent interatomic distances in the sample.

133 Park et al. (2010) describe two other methods for crystallinity determination
134 by diffraction: amorphous subtraction and peak deconvolution. The amorphous

subtraction method, as in the case of Segal's peak height method, depends on the assumption that the diffraction intensity at the valley between the (110) and (200) peaks is all due to amorphous material, and is thus inherently flawed. The XRD deconvolution method has better fundamentals. However, its implementations suffer because it is typically carried out with curve-fitting software, instead of software written to take into account the specific problems of diffraction data such as preferred orientation and anisotropic crystallite size that are endemic to cellulose samples. Also, only a few strong peaks are usually considered, along with a broad curve that defines the amorphous contribution to the overall intensity. Thus, none of the conventional methods for crystallinity study by diffraction is satisfactory.

In the present work, the Rietveld powder diffraction method is used (Rietveld 1969; Young 1993). This method would seem to be the ultimate approach for diffraction study of cellulose crystallinity and has been applied by a number of researchers including Thygesen et al. (2005), Driemeier and Calligaris (2011), Driemeier (2014), Howell et al. (2011), Chen et al. (2015), Xiaohui et al. (2015), Reyes et al. (2016), Ahvenainen et al. (2016), Duchemin (2017) and Vanderfleet et al. (2018). As also shown in Fig. 1 with the simpler Mercury program, the Rietveld method allows calculation of a theoretical diffraction pattern based on the atomic coordinates of a proposed structure, such as the work of Nishiyama et al. (2002). The question is: what changes to that ideal pattern are

needed to make it agree with the observed experimental result? Changes to compensate for variables such as crystallite size, small deviations in unit cell dimensions, and given a model, the presence of amorphous or other phases are optimized with a least squares fit. Even though Rietveld may be the ultimate approach, it is limited by the relatively small amount of data furnished by crystalline cellulose powders, and the X-ray patterns of progressively amorphous material give less and less information.

Nuclear magnetic resonance spectroscopy also has a strong role in cellulose crystallinity studies. Solid-state NMR spectroscopy (ssNMR) has been extensively employed to determine the polymorphic structure of native, functionalized and genetically engineered cellulose (Atalla and Vanderhart 1984; Harris et al. 2012; Wang and Hong 2016; Wickholm et al. 1998). Cellulose crystallinity can be inferred from the intensity ratio of the area under C-4 peaks arising from the crystalline chains that resonate at 87-90 ppm and the area of the disordered domain that shows broader signals spanning 80-86 ppm (Atalla et al. 1980; Newman and Hemmingson 1990; Larsson et al. 1999). This peak broadening is primarily caused by distinct hydroxymethyl torsion angles of C-6: the disordered regions adopt either *gt* or *gg* conformations while the tightly hydrogen-bonded crystallites of cellulose I adopt the *tg* conformation, a structure that is less energetically favored and rarely observed in other carbohydrates (Phyo et al. 2018; Viëtor et al. 2002;

175 Yang et al. 2018). Further peak complexity exists within each category due to
176 conformational polymorphism, magnetic non-equivalence of glucose units, diverse
177 patterns of chain packing, bundling of multiple microfibrils, and interactions with
178 matrix polymers (Kono and Numata 2006; Newman et al. 2013; Wang et al. 2016).
179 Despite investigation using ssNMR of these complicated structural aspects, an
180 original issue remains and is discussed here. Namely, what is the level of
181 agreement with other spectroscopic or diffraction methods in estimating cellulose
182 crystallinity? Our analyses have been informed by the results given in the
183 accompanying paper (Kirui et al., 2019). In the Supporting Information, an
184 analysis of similar NMR data has been carried out with a more conventional
185 approach in which a model is assumed and the samples were swollen in water prior
186 to measurement.

187 Of course, many other techniques have been applied to studies of cellulose
188 crystallinity, or at least their results have been interpreted based on changes in
189 crystallinity. As mentioned already, FTIR has been frequently employed (Liu and
190 Kim 2015) as has Raman spectroscopy (Agarwal et al. 2016). Application of SFG
191 spectroscopy specifically to ball-milled cellulose is new. Other techniques are used
192 herein to provide a fuller understanding of the effects of ball milling, including
193 microscopy, molecular weight and oxidation to carbonyl groups determined by
194 multidetector GPC after group-selective fluorescence labeling, surface area and

pore size, as well as thermogravimetric analysis. The end of the Results and discussion and the Conclusions sections tie these approaches together.

Experimental

Materials

Cotton balls were purchased from Wal-Mart and chopped in a Wiley mill (Eberbach E3300 mini cutting mill, Eberbach Corp., Belleville, Michigan) until they fell through a 20-mesh screen. Then 5 g portions of the powder were placed in a locally built ball mill (Forziati et al. 1950) running at 1750 rpm. The approximately one liter steel jar was chromium plated and 500 mL of stainless steel balls 0.25 in. (~4 cm) in diameter were employed. The cellulose samples milled for 15 min, 45 min and 120 min were respectively labeled as BMC-15, BMC-45 and BMC-120. The control, Wiley milled cellulose, was denoted as WMC.

Lithium chloride was purchased from JT Baker (Philipsburg, NJ, USA) and ethanol, acetone, and dimethylacetamide (DMAc) were purchased from Sigma Aldrich (St. Louis, MS, USA). All chemicals used in this study were either analytical or reagent grade.

Microscopy

Optical images were obtained with a Zeiss Axioplan polarized light microscope (Thornwood, NY, USA) with an AmScope digital camera (Irvine, CA, USA). Both WMC and BMC samples were dispersed with a pointed tool. The fiber lengths were determined with Image J software (1.41v, US National Institutes of Health, USA).

The samples were also observed with an FEI Quanta 3D FEG Field emission scanning electron microscope (FE-SEM, Hillsboro, Oregon, USA). The accelerating potential was 5 kV, with a beam current of 20 mA. The samples were sputter coated with a 3-nm layer of gold–palladium using a Leica EM ACE600 (Buffalo Grove IL, USA).

Molecular weight determination and carbonyl group analysis

The samples were treated according to a standard protocol (Röhrling et al. 2002) for cellulose labelling (7 days in a shaking water bath at 40°C). After solvent exchange from water to ethanol into DMAc the samples stayed 12 h in DMAc, were dissolved in DMAc/LiCl 9% and diluted with DMAc prior to injection. The raw data are available upon request. The degree of polymerization was calculated by the following equation:

$$DP = M/162 \qquad (1)$$

where M is the molecular weight of each sample and 162 is the molecular weight of an anhydroglucose unit. The maximum molecular lengths (N) were obtained by:

$$N\ (nm) = DP*0.5125 \qquad (2)$$

where 0.5125 is our estimated advance per glucose residue along an extended but non-symmetric molecule.

Surface properties and thermal analysis

The specific surface area (SSA) and pore sizes of the ball-milled cotton cellulose were measured using Brunauer, Emmet and Teller nitrogen adsorption (Brunauer et al. 1938; Sehaqui et al. 2011) using a TriStar II Plus 2.02 Analyzer (Service purchased from Particle Testing Authority, Norcross, GA, USA). Prior to analysis, samples were under vacuum at 150 °C.

For thermogravimetric (TGA) and differential thermogravimetric (DTG) analyses, all cellulose samples (5 mg each) were conditioned in a Nor-Lake Scientific humidity chamber at 60 °C overnight (Hudson, WI, USA). Tests used a TA Q500 thermogravimetric analyzer (TA Instruments, New Castle, DE) and a nitrogen atmosphere. Samples were heated from 0–600 °C at a rate of 10 °C/min. Thermograms were analyzed by the Universal Analysis 2000 Software (TA Instruments).

Spectroscopy

FTIR spectra were collected on a Vertex 70 (Bruker Optics, Billerica, MA) equipped with a mid-IR source and an attenuated total reflection (ATR) sampling accessory (Pike Technologies, Madison, WI) with a diamond-ZnSe crystal. Samples were placed on top of the ATR crystal and secured with a metal clamp in a manner that assured consistent pressure for all samples. Three measurements were performed for each sample, with a total of 128 scans taken for each sample at a resolution of 4 cm^{-1} (3800 – 600 cm^{-1}). Spectra were corrected against an air background. Spectra for each sample were averaged, baseline-corrected and normalized using the OPUS spectroscopy software (version 6.5). Spectra are presented without ATR correction or atmospheric compensation.

The FT-Raman spectra were collected using a DXR2 785 nm Raman microscope (Thermo Fisher Scientific Inc., USA). The spectra (100-3100 cm^{-1}) were obtained with a laser power of 10 mW, exposure time 1 s with a 25 μm pinhole aperture. Each spectrum was measured once with an accumulation time of 10 s. Spectra were collected by OMNIC for Dispersive Raman software (Thermo Fisher Scientific).

For vibrational SFG spectroscopy, the samples were pressed into pellets. Details of the SFG system have been discussed extensively elsewhere (Lee et al. 2015a). Briefly, SFG beams were generated by spatial and temporal overlap of

800-nm and IR laser beams. A Ti-sapphire amplifier (Coherent, Libra) generated 800-nm laser pulses that were then narrowed by using two Fabry-Pérot etalons to 0.78 nm width. A broadband-tunable IR beam (1000 – 4000 cm^{-1}) with full width at half maximum (FWHM) of 150-200 cm^{-1} is generated using an optical parametric generation/amplification (OPG/OPA) system (Coherent, OPerA Solo). The analysis was carried out with p-polarized IR and s-polarized 800 nm, and the s-polarized SFG signal was recorded. The experiment was done with reflection geometry with two laser beams (IR and 800 nm) shining on samples with a 45° angle. The generated SFG beam was passed through a monochromator and detected by a CCD camera. To minimize the heterogeneity in samples, the spectra were collected from ten randomly chosen locations on the pellets and averaged. Each spectrum was normalized by the IR power.

Solid-state NMR experiments

For the conventional solid-state NMR experiments, 50-59 mg of the native and ball-milled cotton samples were directly packed into 4-mm zirconium rotors for measurements. Solid-state experiments were conducted on a 400 MHz (9.4 Tesla) Bruker Avance spectrometer (Bruker Optics, Billerica MA, USA) using a 4-mm MAS HCN probe. The standard ^{13}C CP experiments were collected under 10 kHz magic-angle spinning (MAS) at 296 K. ^{13}C chemical shifts were externally

294 referenced to adamantane CH_2 signal at 38.48 ppm on the TMS (tetramethylsilane)
295 scale. Typical radiofrequency field strengths were 80 kHz for ^{1}H decoupling and
296 hard pulse, 62.5 kHz for 1H and ^{13}C CP. A contact time of 1 ms is used for CP. For
297 signal averaging, 12288 scans were measured on each sample. The spectra were
298 deconvoluted using DMfit software (Massiot et al. 2002). The WMC and BMC
299 samples were also processed using a matrix-free protocol for DNP experiments
300 (Takahashi et al. 2012) and the results are detailed in an accompanying separate
301 paper (Kirui et al. 2019).
302
303 **Diffraction experiments**
304 Laboratory XRD measurements were performed at room temperature with a
305 PANalytical Empyrean laboratory diffractometer (Malvern Panalytical Inc.,
306 Westborough MA, USA) with a spinning, zero-background sample holder, using
307 Cu Kα-radiation and a PIXcel3D detector. The patterns were corrected by a blank
308 and then analyzed using the pseudo-Voigt peak shape with the MAUD Rietveld
309 program (Materials Analysis Using Diffraction, version 2.7, Lutterotti et al. 2007).
310 The crystallinity was calculated from the area of the calculated pattern for
311 crystalline cellulose divided by the sum of the areas for crystalline and amorphous
312 regions. The *d*-spacings were calculated from refined unit cell dimensions, and

crystallite sizes perpendicular to different lattice planes were calculated using the Scherrer Equation (3).

$$L_{hkl} = \frac{0.9\lambda}{B_{hkl}\cos\theta} \qquad (3)$$

where λ is the X-ray wavelength, B_{hkl} is the angular FWHM in radians of the (hkl) line profile, and θ is the scattering angle (Holzwarth and Gibson 2011).

Synchrotron measurements were performed at beamline 6B of the Center for Advanced Microstructures and Devices (CAMD) (Baton Rouge, Louisiana, USA). Samples of 1 mg of milled cotton were placed in a plastic capillary (MiTeGen MicroRT, Ithaca NY) for which the background scattering pattern was individually recorded immediately prior to filling and collecting the data. Exposure time was 10 s and wavelength λ=1.38 Å. The MAR 2048 x 2048 CCD detector synchrotron data were visualized and converted to 1D data with the XRD2D Scan software (Rodriguez-Navarro 2006). The Caglioti asymmetry parameters in the MAUD Rietveld program were adjusted from their Bragg-Brentano defaults (used with the laboratory data) to zero, and the HWHM Caglioti value0 was set to 0.00025; the value1 and value2 parameters were set to 0.

For visual comparison (Figs. 9 and 10), the synchrotron X-ray patterns (λ=1.3801Å) were converted to the same 2θ scale as the laboratory data (λ=1.5418 Å) by solving the Bragg equation (4) (Klug and Alexander 1974) for *d*

$$n\lambda = 2d\sin\theta \qquad (4)$$

and then converting the *d* value to 2θ with the Bragg equation's arcsin inverse.

Results and discussion

Optical microscopy and FE-SEM

Polarized light optical micrographs of the samples are in Fig. S1. Previously immersed and dispersed in alcohol, many particles in the WMC and BMC-15 samples were birefringent under polarized light. WMC showed intact and long cellulose fibers with an average length of 296 μm. Ball milling for 15 min broke

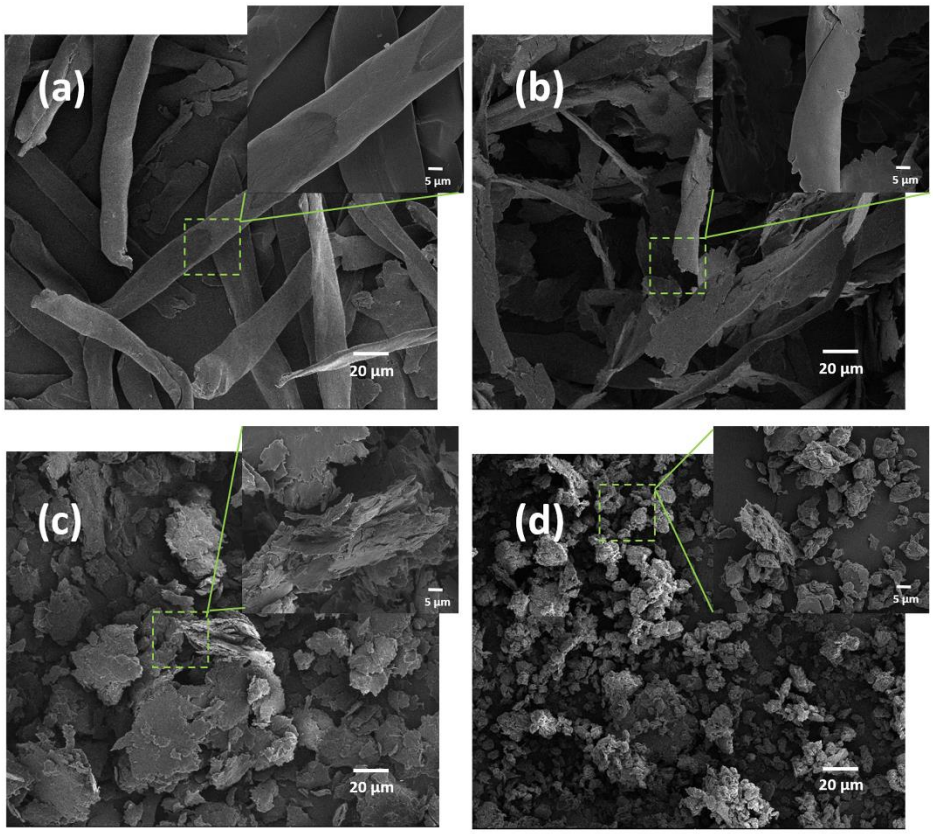

Fig. 2 SEM images of Wiley milled cotton (a) and cotton ball-milled for 15 min (b), 45 min (c) and 120 min (d). Scale barsin large images and insets = 20 μm and 5 μm respectively

down the fibers, lowering the sample birefringence as well as the average size of fibers. With longer milling time, the fiber shape disappeared for BMC-45 and BMC-120 (average sizes were 47 μm and 23 μm, respectively), indicating that the extended ball milling effectively broke the WMC fibers into smaller particles.

Figure 2 shows the FE-SEM images of the samples. Wiley milling chopped the cotton fibers into relatively large fragments of about 120 μm in length (Fig. 2a). A closer observation of a single fiber (zoomed in Fig. 2a) shows that the intrinsic fiber morphology of WMC remained intact. However, ball milling significantly degraded the fiber. Even 15 min of ball milling (Fig. 2b) split open some fibers along the fiber length as well as breaking some into small fragments. The fragments were irregular, but the longitudinal fragmentation was dominant. Ball milling extended to 45 min reduced the aspect ratio of the fragments to generate particles with a diameter of about 50 μm (Fig. 2c). However, some large particles remain in sample BMC-45, suggesting the inhomogeneity of cellulose fiber particles after ball milling. The size of the particles was further decreased to about 7 μm after 120 min of ball milling (Fig. 2d). The disordered fiber residues were

372 approximately 10-15 μm in length (zoomed in Fig. 2d) with coarse surfaces and
373 pores, showing the higher extent of destruction of the cotton fibers.
374
375 **Molecular weights**
376 Table 1 shows that the molecular weights of the samples decrease steadily with
377 increased milling time. Some oxidation is revealed by the notably increased
378 carbonyl amount from 1.9 μmol/g (WMC) to 36 μmol/g for BMC-120. As the
379 chains became shorter, more carbonyl groups per unit mass appeared than the
380 expected increase based on the increased number of reducing ends from breakage
381 of the molecules. However, the oxidation resulted in only more carbonyls, whereas
382 the amount of uronic acid groups did not increase significantly. The distributions
383 of oxidized functionalities with regard to molar mass and the corresponding molar
384 mass distributions are given in Fig. S2.
385
386 **Table 1** The DP based on number-average molecular weight (Mn), weight-average
387 molecular weight (Mw), Z-average molecular weight (Mz); sample polydispersity
388 and calculated average molecular lengths of Wiley and ball-milled cotton cellulose

Samples	DP on number-average (Mn) [a]	DP on weight-average (Mw)	DP on Z-average (Mz)	Dispersity (Mw/Mn) [b]	Molecular lengths (nm) from Mn, Mw, Mz [c]
WMC	718	3335	5850	4.7	370 / 1718 / 3013

BMC-15	517	2143	4696	4.2	266 / 1103 / 2418
BMC-45	344	1409	3659	4.3	177 / 726 / 1885
BMC-120	265	856	2134	3.2	137 / 441 / 1099

[a] DP was calculated by equation (1)

[b] The dispersity equals Mw/Mn.

[c] The molecular lengths were calculated according to equation (2).

Specific surface area (SSA), pore size and thermogravimetric analysis (TGA)

SSA was determined from N_2 adsorption using BET analysis (Brunauer et al. 1938; Sehaqui et al. 2011). All samples presented similar adsorption isotherm curve shapes (Fig. 3a). WMC absorbed the lowest quantity of N_2. The highest absorption value was 5 cm^3/g for BMC-120. The SSA and average pore width are plotted in Fig. 3b based on the BET analysis. SSA showed a gradual increase with increased ball milling time. It can be explained by the destruction of cellulose structures after ball milling and exposure of internal surface of fibers as seen in the SEM images (Fig. 2).

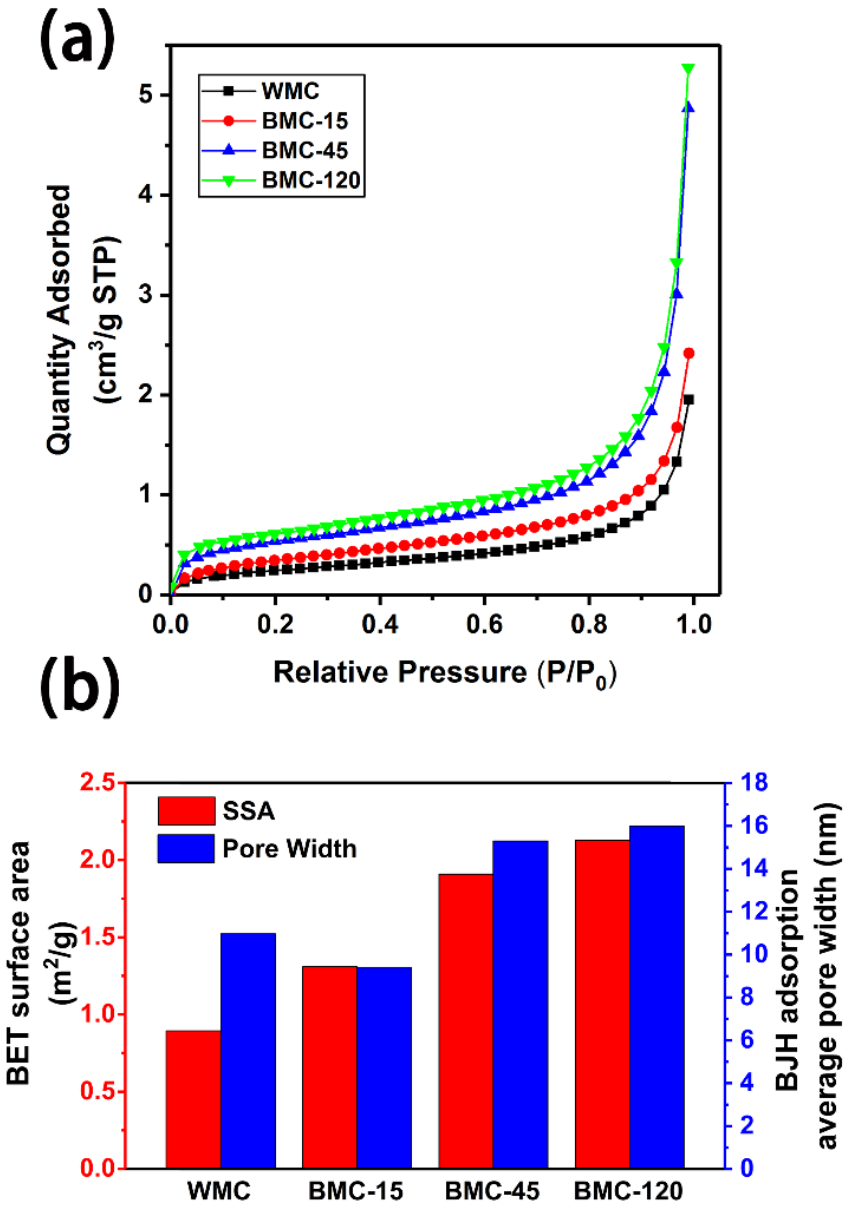

402

403 **Fig. 3** The adsorption isotherms (a) and BET surface area (red bars in b), BJH

404 adsorption average pore width (blue bars in b) of Wiley milled cotton cellulose and

405 cotton cellulose ball milled for 15, 45 and 120 min

406

The average pore width decreased slightly for BMC-15 but the pores were opened significantly for BMC-45 and BMC-120 with approximately 15 nm of average pore width. As expected, the ball-milling treatment for longer times is an effective way to disrupt the ordered arrangements of cellulose molecules. It breaks down the fibrous structures, exposes more surface area, and opens the pores of cotton. The initial decrease in pore size may have resulted from impact compression by the ball mill without the damage and fragmentation that occur at longer ball-milling times.

The samples were studied by TGA and DTG under an N_2 atmosphere. All data were plotted in the TGA weight loss mode and the DTG mode. From the analysis of thermal properties, we can estimate the cellulose crystallinity according to Bertran and Dale (1986), who used DSC to show that the crystallinity of cellulose could be correlated with the moisture content. The hypothesis was that the amorphous region of cellulose should absorb more moisture in a humidity chamber, whereas the crystalline region adsorbs much less. Of course, there is a rough correlation between the initial moisture content and SSA.

The TGA and DTG results are displayed in Fig. 4. The point of rapid weight loss for WMC appeared at nearly 300 °C while the curves for BMC samples shifted left to lower temperatures (Fig. 4a). BMC-120 began degrading obviously at 250 °C and lost almost all of its initial weight, indicating a decrease of thermal

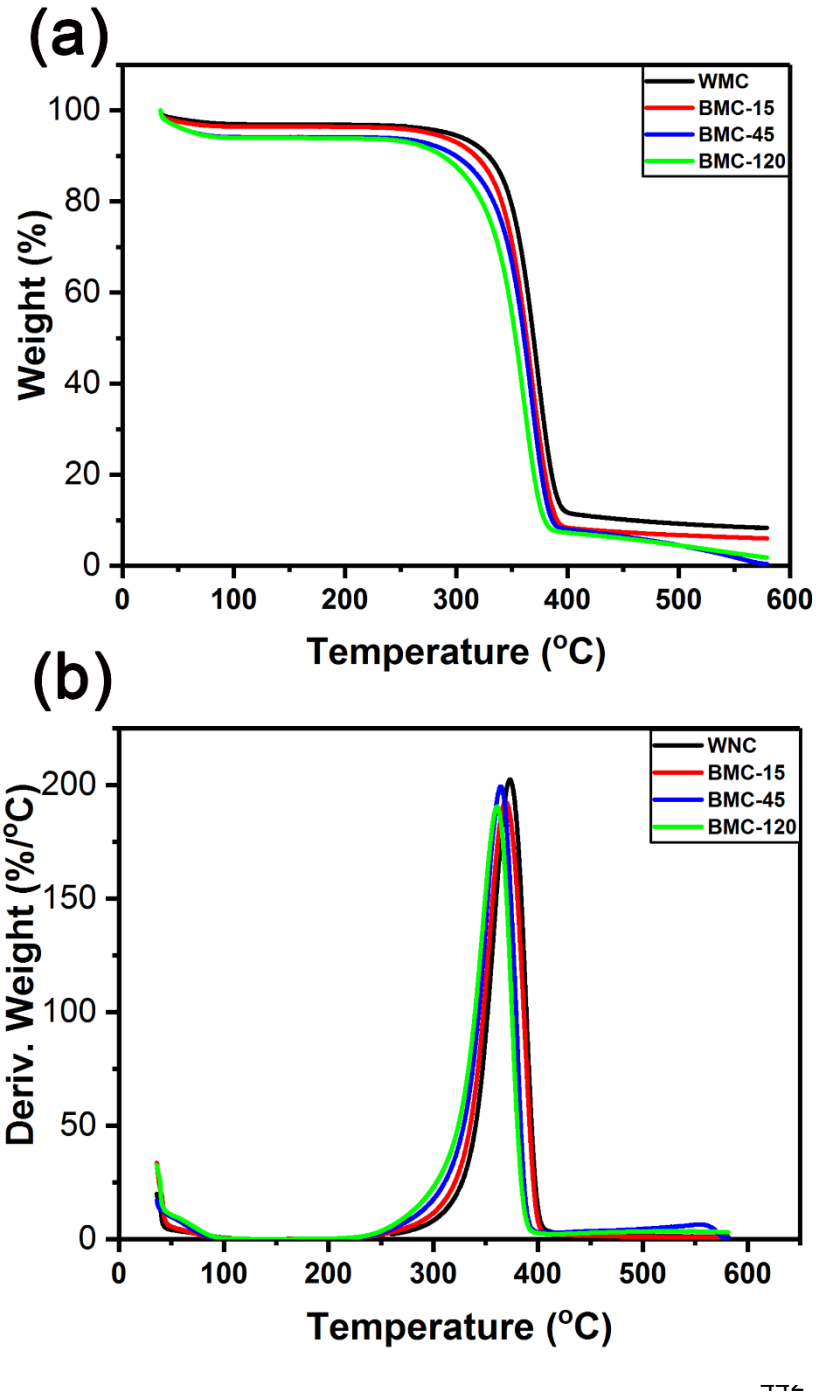

443

444 **Fig. 4** TGA (a) and DTG (b) analyses of Wiley milled cellulose and ball-milled

445 cellulose for different times

446 stability after ball milling. WMC showed the highest maximum degradation rate as
447 well as the highest degradation temperature (Fig. 4b). With extension of ball-
448 milling time, the temperature for maximum degradation rate reduced to 369.3 °C,
449 367.2 °C and 362.4 °C for BMC-15, 45 and 120 (Fig. S3a). However, the weight
450 loss at each maximum DTG temperature showed a gradual increase (Fig. S3b),
451 confirming the loss of stability after ball-milling treatments. This apparent loss
452 could result, however, from a constant heating rate and the smaller particle sizes of
453 the ball-milled materials. If the weight loss is taking place on the surfaces, larger
454 crystals would take a longer time to decompose.

455 Two more correlations are shown for the four cotton samples (Fig. S4). The
456 plots give the correlation of weight loss at 100 °C versus the temperature at the
457 maximum degradation rate as well as the weight loss vs the maximum degradation
458 rate. Both correlations are satisfactory (R^2 = 0.99 and 0.94, respectively) for the
459 cellulose samples that were preconditioned in the humidity chamber. The good
460 correlations of the ball-milling time duration with two parameters further suggest
461 that the high moisture loss is from the amorphous material of BMC.

462

463 **ATR-FTIR and FT-Raman spectroscopy**

464 The FTIR spectra are shown in Fig. 5a. The spectrum for WMC showed infrared
465 bands and peaks commonly observed for cotton: a wide OH stretching band (3600-

466 3000 cm^{-1}), a CH stretching region (3000-2900 cm^{-1}), the OH bending region,
467 1800–1300 cm^{-1}, and the fingerprint region with multiple combination bands,
468 1250–850 cm^{-1}. The visible bands at 3270 cm^{-1} and 710 cm^{-1} are typical for
469 cellulose Iβ for WMC, even though there are tiny peaks at 3240 cm^{-1} and 750 cm^{-1}
470 assigned to a small amount of cellulose Iα (Sugiyama et al. 1991). Ball milling
471 leads to progressive broadening of the OH band, with the BMC-120 spectrum
472 lacking the inflection points at 3334 cm^{-1} observed for WMC. Meanwhile, the
473 bands attributed to both cellulose Iα and Iβ disappeared for BMC-120, a result
474 attributed mainly to the destruction of the crystal structure by lengthy ball milling.
475 Ball milling also results in changes to the fingerprint IR region. While the
476 position of the 1159 cm^{-1} peak is slightly altered by ball milling, its intensity
477 appears unaffected. In contrast, the well resolved peaks at 1107 and 1052 cm^{-1}
478 diminish in intensity for the sample ball-milled for 120 min. The prominent peak at
479 1029 cm^{-1} is gradually shifted to 1019 cm^{-1} following ball milling. Two shoulder
480 bands are observed centered at 1000 and 985 cm^{-1} in the Wiley milled sample;
481 however, only one shoulder band (995 cm^{-1}) is observed for BMC-120. The peak
482 near 898 cm^{-1} appears more intense in the ball-milled cotton samples. An early
483 study by Nelson and O'Connor (1964b) observed similar spectral changes in ball-
484 milled cotton samples. Key changes include the position of the 1163 cm^{-1} band
485 (observed in this study at 1159 cm^{-1}), and the intensity of bands at 1111 and 893

cm^{-1} (observed in this study at 1107 and 898 cm^{-1}, respectively). Their study did not show significant changes to the 1052, 1000 and 985 cm^{-1} bands, but these

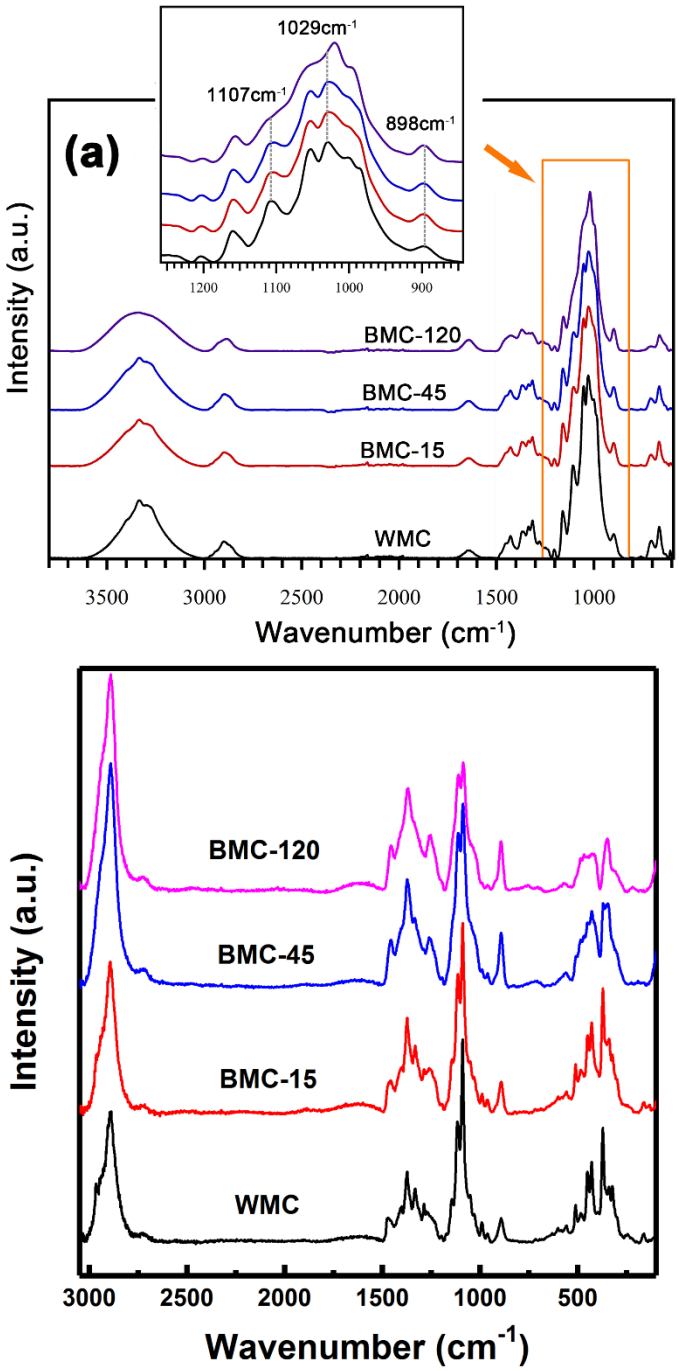

Fig. 5 ATR-FTIR (a) and FT-Raman (b) spectra of Wiley milled cellulose, and cellulose ball-milled for 15 min, 45 min and 120 min. A small peak for water in amorphous domains is seen at ~ 1650 cm^{-1}.

differences could be the result of their sampling methodology and resolution of their instrument.

The Raman spectra of Wiley and ball-milled cotton cellulose are presented in Fig. 5b. With the increase of milling time, the main peak of cellulose at 380 cm^{-1} assigned to symmetric bending vibration of pyranose rings in crystalline cellulose showed visible reduction together with the C-O-C and C-H stretching vibration at 1096 cm^{-1} and 2900 cm^{-1}, respectively (Agarwal and Ralph 1997; Agarwal et al. 2016; Makarem et al. 2019). The decreases of these main peaks were substantial for BMC-120, indicating the distortion of crystalline arrangements and the smaller CrI. Meanwhile, the peaks attributed to the bending vibrations of cellulose glycosidic linkages (990 cm^{-1}, 1116 cm^{-1} and 1331 cm^{-1}) disappeared for the most amorphous sample (BMC-120) (Wiley and Atalla 1987).

The notable peak of 1481 cm^{-1} in WMC shifted to 1462 cm^{-1} with prolonged ball milling. The ratio of these two peaks refers to the proportion of crystalline cellulose, and confirmed an increased amorphous fraction in the sample, leading to a significant decrease of CrI (Schenzel et al. 2005).

SFG analysis

SFG spectroscopy is specific to non-centrosymmetric vibration modes in an otherwise amorphous matrix (Barnette et al. 2011). The SFG signal intensity can be used to quantify the amount of crystalline cellulose in the sample if a proper calibration curve can be obtained (Barnette et al. 2012; Park et al. 2013). For ball-milled cellulose, the main features observed in the CH stretch region (2800-3000 cm^{-1}) are the peak at 2850 cm^{-1} assigned to the CH_2 symmetric vibration, the peak at 2944 cm^{-1} as the CH_2 asymmetric vibration, and a shoulder at 2968 cm^{-1} also assigned to CH_2 asymmetric vibrations (Fig. 6a) (Lee et al. 2013). Time-dependent density functional theory (TD-DFT) calculations also revealed that the CH_2 vibrations between 2800-3000 cm^{-1} are highly coupled with CH vibrations on the six-atom ring (Lee et al. 2016a). Thus, the peaks in this region represent more than just the vibrational modes of isolated CH_2 groups. The peak at 2944 cm^{-1} is characteristic for cellulose Iβ, which also has a shoulder at 2968 cm^{-1} (Huang et al. 2018a). With increased ball-milling time, peaks between 3200-3500 cm^{-1} assigned to the stretching vibrations of OH groups in cellulose Iβ show a notable decrease. Note that OH peaks in this region also cannot be assigned to single vibrational modes; they originate from highly coupled vibrations of multiple OH groups in cellulose structure (Lee et al. 2015b). Meanwhile, the broad component at 3450

546 cm^{-1} can be attributed to OH groups exposed at the surface of cellulose crystals
547 (Makarem et al. 2017).

548 Fig. 6b displays changes in the total intensity of the CH/CH_2 SFG peak as a
549 function of ball-milling time. The SFG intensity from the cellulose Iβ phase in the
550 BMC-15, -45, AND -120 samples decreased to ~35%, ~9%, and ~1%,
551 respectively, compared to the SFG intensity of WMC. This implies that a small
552 fraction of cellulose Iβ crystallites still remains in BMC-120.

553 Another important aspect is that the shape of the CH/CH_2 asymmetric stretch
554 feature in the 2900-3000 cm^{-1} region changes with ball milling. The relative
555 intensity ratio (2968 cm^{-1}/2944 cm^{-1}) is plotted against the right-side red axis in
556 Fig. 6b. The increase in this ratio implies that a small fraction of cellulose Iβ was
557 converted to cellulose II, as also found for the FTIR work. This transformation
558 might have happened when the amorphized portion of cellulose chains underwent
559 crystallization due to the proximity of cellulose chains or mechanochemical
560 processes during ball milling.

561 SFG peaks in the OH stretch region (3200-3600 cm^{-1}) can be deconvoluted
562 with various components. The component at 3270 cm^{-1} is characteristic of cellulose
563 Iβ. The fraction of this component intensity with respect to the entire OH
564 components (f_β) can show the change in cellulose I_β fraction among the SFG-active

565 fraction of cellulose. The plot of f_β versus the milling time is also shown in Fig. 6b,

566 decreasing as the ball-milling time increases.

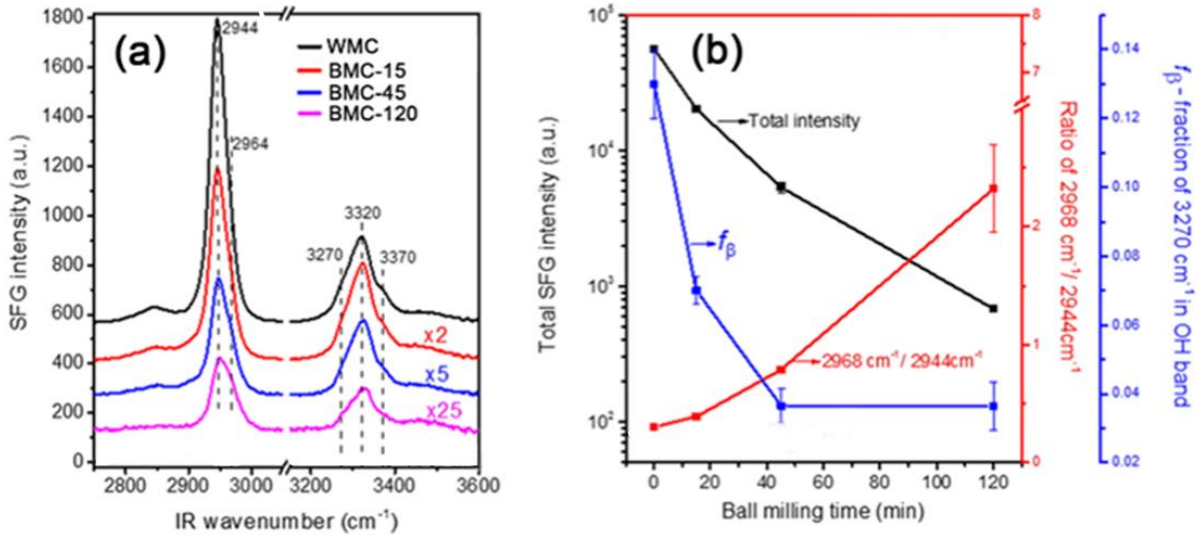

567

568 **Fig. 6** (a) SFG spectra of cotton before and after ball milling for 15 min, 45 min,

569 and 120 min. Note that some spectra are amplified for comparison with different

570 magnification ratios (marked for each spectrum). (b) Plots of the SFG total

571 intensity, the 2968cm^{-1}/2944cm^{-1} intensity ratio, and the 3270 cm^{-1} fraction in the

572 OH peak versus the ball-milling time

573

574 **NMR characterization**

575 The standard ^{13}C CP spectra of WMC and the three BMC samples show that

576 cellulose crystallinity decreases with longer ball milling by the sequential

reduction in the intensity of crystalline cellulose C-4 at 88-90 ppm and the rise of disordered cellulose C-4 at 80-85 ppm. Peak multiplicity was observed in WMC since both Iα and Iβ cellulose contain two magnetically inequivalent glucose units: A and A' for Iα and B and B' for Iβ (Fig. 7) (Kono and Numata 2006). For BMC-45, the sharp peaks become negligible: instead, the spectra are dominated by broad components originating from the disordered forms (D), the intensity of which was low in the Wiley milled sample.

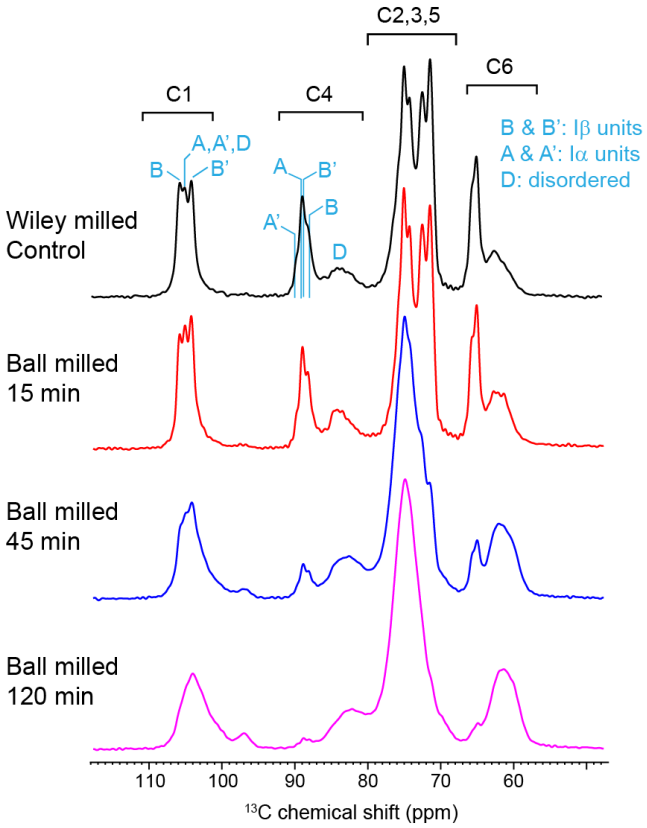

Fig. 7. ^{13}C CP spectra of Wiley milled control and ball milled cotton samples. Representative signals of the inequivalent glucose units in Iα and Iβ cellulose are labeled in cyan for the control sample

588

589 Spectral deconvolution allows us to analyze the composition and
590 crystallinity of cellulose in greater detail and as a function of ball-milling time. The
591 peak positions are using those resolved in the 2D ^{13}C-^{13}C correlation spectra of
592 these unlabeled samples as enabled by the sensitivity-enhancing Dynamic Nuclear
593 Polarization (DNP) technique, the spectral and technical details of which are
594 reported in a separate article in the same issue (Kirui et al. 2019). The simulated
595 and measured spectra dovetail well (Fig. 8a). In contrast, the central peak position
596 for the disordered part gradually shifted from 85 ppm in WMC to 82 ppm in
597 BMC-120. Quantification of peak areas shows that the cellulose crystallinity
598 decreases in the order of 68%, 58%, 28% and 13% in the four samples, which
599 clearly reveals the molecular-level structural effect of ball milling (Fig. 8b).
600 A central question is whether the crystallites of cellulose fracture
601 homogeneously or not. This was addressed by monitoring the intensity change for
602 the highly disordered form (Hd) at 82.5 ppm, which is only a minor component in
603 the Wiley milled cotton but becomes dominant after 2 h of ball milling, accounting
604 for one-fifth of all cellulose (Fig. 8c). If structural fractioning of the crystallites
605 occurs progressively, we expect the size of cellulose particles to be roughly
606 consistent within each step, a scenario in which the most disordered molecular
607 structures can only occur in the last step (Fig. 8d). In contrast, linear growth of the

highly disordered subform is expected for inhomogeneous fractioning, in which large and small particles could coexist. The experimental results align better, although not perfectly, with the second model, suggesting that cellulose crystallites are perturbed inhomogeneously during the ball-milling process. This concept of inhomogeneous decrystallization is also supported (at a much larger length scale) by the imaging results presented in Fig. 2 and Fig. S1.

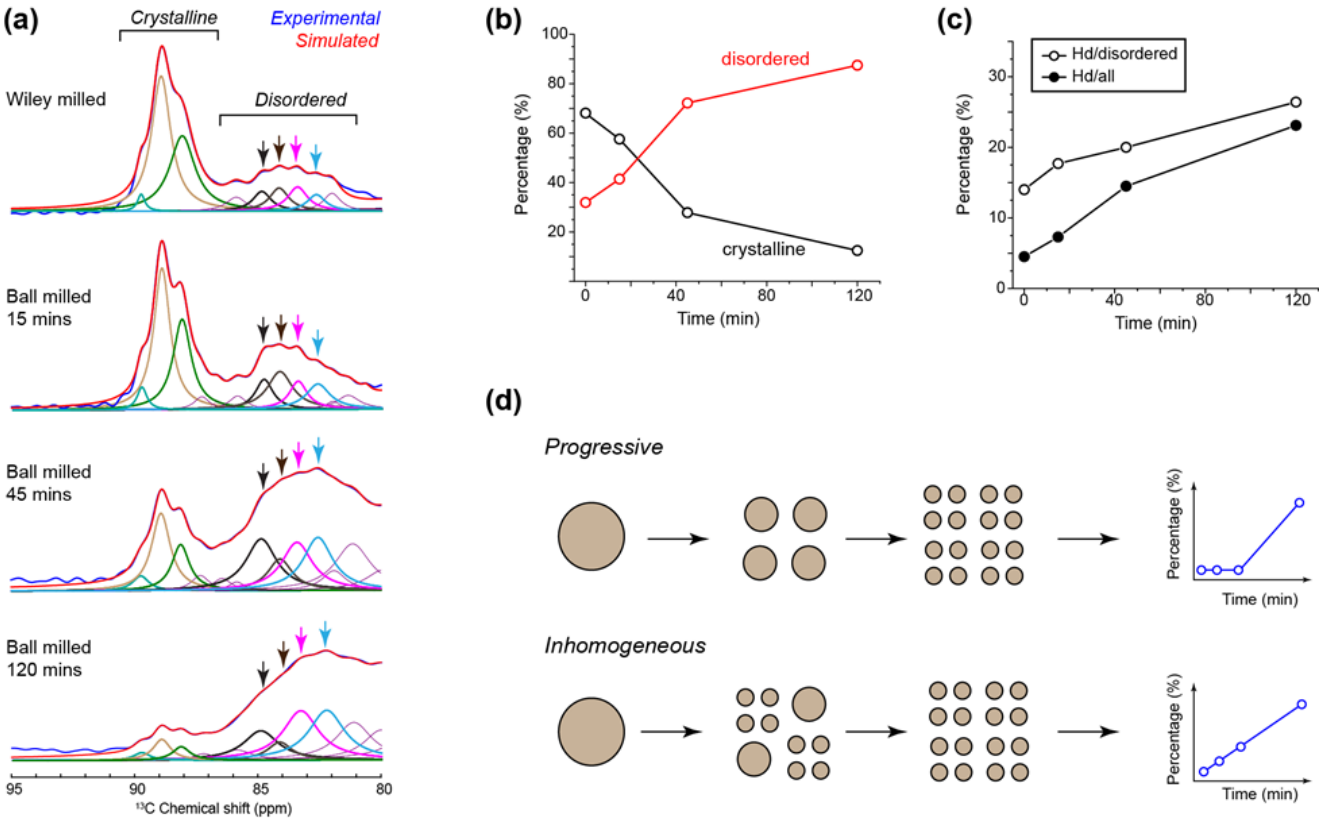

Fig. 8. Compositional change of cellulose during ball milling. (a) Cellulose compositional change tracked by spectral deconvolution. (b) Quantification of cellulose crystallinity. (c) The content of highly disordered (Hd) allomorph (82.6 ppm) increases with longer duration of ball milling. (d) Two models for cellulose

619 fractioning during ball milling. The NMR data in panel (c) support inhomogeneous
620 fractioning

621

622 **Laboratory and synchrotron X-ray diffraction analyses**

623 Because of the fundamental problems with the conventional methods (see
624 Introduction), we have used only the Rietveld method to analyze the crystallinity
625 of the samples. Crystallinity was analyzed with laboratory (reflection mode) and
626 synchrotron (transmission mode) X-rays. All data were corrected by subtracting
627 background due to the air scatter and sample holder and, for the synchrotron work,
628 the capillary. The patterns are compared in Fig. 9. WMC gave typical cellulose Iβ
629 X-ray patterns with major peaks at 14.8°, 16.5°, 22.5° and 34.5°, respectively
630 attributed to the (1-10), (110), (200) and (004) reflections (Fig. 1 shows that each
631 of these peaks [especially (004)] is a composite of one or more adjacent peaks.)
632 The slightly lower 2θ value (22.5°) for the (200) reflection of the control cotton
633 compared to the 23.0° value for the archetype tunicate structure indicates a larger
634 d-spacing, perhaps resulting from the reduced long-range forces in the smaller
635 crystallites of cotton. Also, there may be strains on the crystallites because of their
636 participation in the complex cell wall architecture that results in a disrupted
637 structure compared to the higher order of the tunicate nano-needle crystallite films
638 (see Fig. 6 in Huang et al., 2018b). The synchrotron X-ray pattern of WMC

(WMC-S in Fig. 9) presents a few more peaks than the laboratory pattern WMC-L. The two overlapping peaks at 20.3° and 20.6° are assigned to the (012) and (102) reflections (Fig. 1). The near absence of those "shoulder" peaks near the (200) peak on the WMC-L pattern indicates preferred orientation of the crystallites (French 2014) despite the sample simply being sprinkled on the diffractometer's rotating sample holder and pushed towards the center with a spatula.

As the ball milling progressed, the maximum intensity decreased for these patterns (Fig. 9), which are plotted with constant areas between the curve and the baselines (not shown). Instead, the photon counts (X-ray intensity values) were slightly higher in most places to compensate for reduced (200) peak height. Under these conditions of constant (intensity × 2θ°) area it is legitimate to state that higher peaks indicate higher crystallinity. The pattern for BMC-120 is similar to those in studies on amorphous cellulose produced with different kinds of solvents (Schroeder et al. 1986; Isogai and Atalla 1991; Rollin et al. 2011).

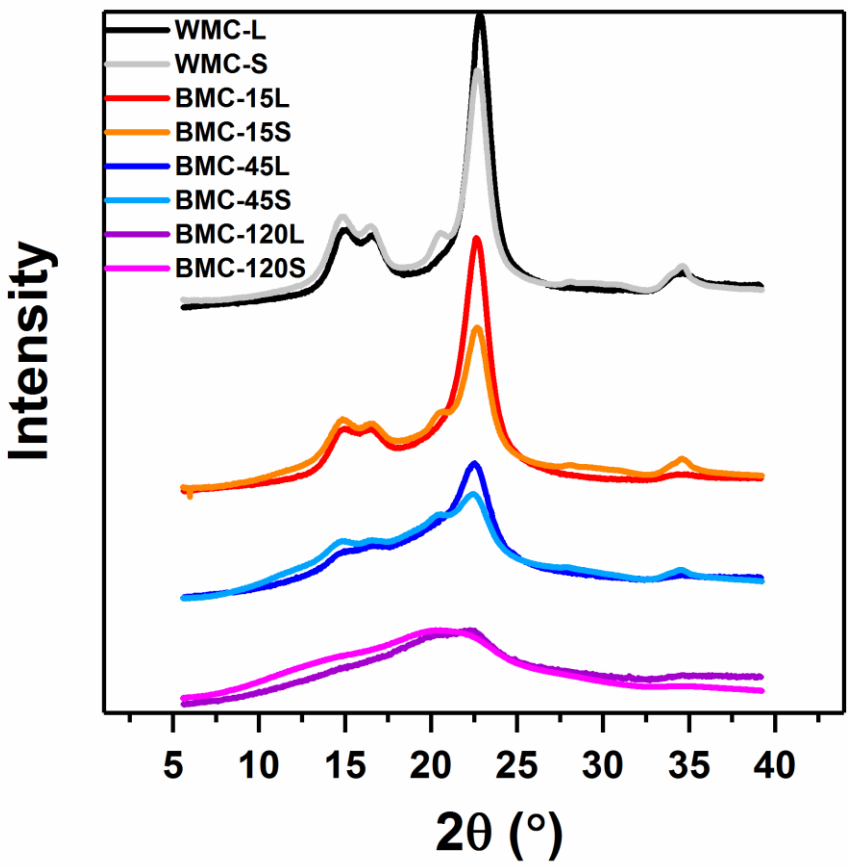

665

666 **Fig. 9** Laboratory (L) and CAMD synchrotron (S) X-ray patterns for the samples.
667 For comparison, the intensities were adjusted to have comparable area under the
668 curves, with compensation for the different wavelengths and step sizes

669

670 Rietveld analyses were performed to obtain more detailed information from
671 laboratory and synchrotron X-ray patterns (Fig. 10). All the samples show fairly
672 good fits of the calculated patterns to the experimental patterns in the images a-h.

673 The thin red lines (representing the crystalline Iβ component) indicate reduced
674 peak heights and areas under the curve as the ball-milling time increased.
675 Meanwhile, the areas under the green lines, representing the quantity of amorphous
676 cellulose, were progressively greater proportions of the total. The crystallinity
677 index (CrI) values calculated from the Rietveld refinement are also shown in Fig.
678 10. WMC had CrI values of 88.7% for the laboratory XRD data and 62.1% for the
679 synchrotron data. The relatively lower value of CrI from the synchrotron analysis
680 is possibly a consequence of the inhomogeneity of the sample. Particle sizes were
681 not uniform. Importantly, these crystallinity values are based on values of intensity
682 for the calculated components exported from MAUD. MAUD also presents
683 percentages of each phase in the program interface with typically very high error
684 limits. Those values can differ substantially from the percentages calculated from
685 the areas under the curves plotted in Fig. 10. Rietveld CrI analyses of BMC-15 and
686 BMC-45 gave similar values regardless of X-ray source (laboratory and
687 synchrotron). Those CrI are around 50% and 30% respectively. The amorphous
688 phase dominated the patterns for BMC-120, with fairly similar CrI values of 13.2%
689 and 5.2%. As in the SFG and NMR results, X-ray diffraction indicates that not all
690 of the cellulose I crystallinity was destroyed even after 120 min. This is in contrast
691 to the conclusions of Millett et al. (1979) who obtained similar diffraction patterns
692 and used the Segal method. Comparison of the BMC-120 patterns in Fig. 9 and 10

693 emphasizes how the visual impression of the nature of the diffraction pattern can
694 change depending on the amplitude of the y-axis for intensity. The Rietveld
695 method is immune to visual impressions and it gave results for BMC-120 that are
696 more consistent with the SFG and ssNMR results.

697 The 2D synchrotron X-ray diffraction images are also shown in Fig. 10 to
698 the right of the 1D patterns obtained from the XRD2DScan program. The black
699 experimental line in Fig. 10b (underneath the blue fitted line), for example can be
700 considered to be the result of scanning to the right from the center of the adjacent
701 2D pattern. The 2D image of BMC-15 shows an uneven intensity distribution
702 proceeding around the rings at the same 2θ angle (Fig. 10, row 2). This is another
703 example of preferred orientation, which occurred for the sample in the capillary
704 tube for the synchrotron. The pattern is very similar to those from cotton fiber
705 bundles (French and Kim 2018) although the sample consisted of particles picked
706 up with tweezers and pushed into a capillary tube. (It was difficult to ensure good
707 sampling for these small samples.) This underscores the need to take measures to
708 avoid preferred orientation and to be aware that it may be inconsistent from sample
709 to sample. In the present laboratory experiments, the sample holder was rotated
710 during data collection. In the synchrotron experiments, the data were averaged
711 around each circle to get the 1D plots.

712 In this work, the amorphous material was modeled by a very small crystal of
713 cellulose II (Langan et al. 2001), initially 12 Å in each direction. The calculated
714 scattering is somewhat different from that of cellulose Iβ and seem to fit the
715 observed data better. Rietveld refinements that include this model for amorphous
716 material can vary the same parameters as are varied for the crystalline phase,
717 providing the needed variability to compensate for differences in amorphous
718 material.

719 In our earlier Rietveld analyses of cellulose, we had not corrected the
720 experimental data for the background scattering. In those cases, the background
721 was instead included as part of the Rietveld refinement, based on a quadratic
722 equation. In a number of cases, the refined amorphous component of the calculated
723 intensity and the refined background worked together to give a better fit to the
724 observed data but the values for the background were negative in some 2θ ranges.
725 Subtraction of carefully collected background data from the experimental data
726 allowed the Rietveld refinement to avoid the unphysical results because the
727 background was simply not included and reduced the number of variable
728 parameters by three.

729

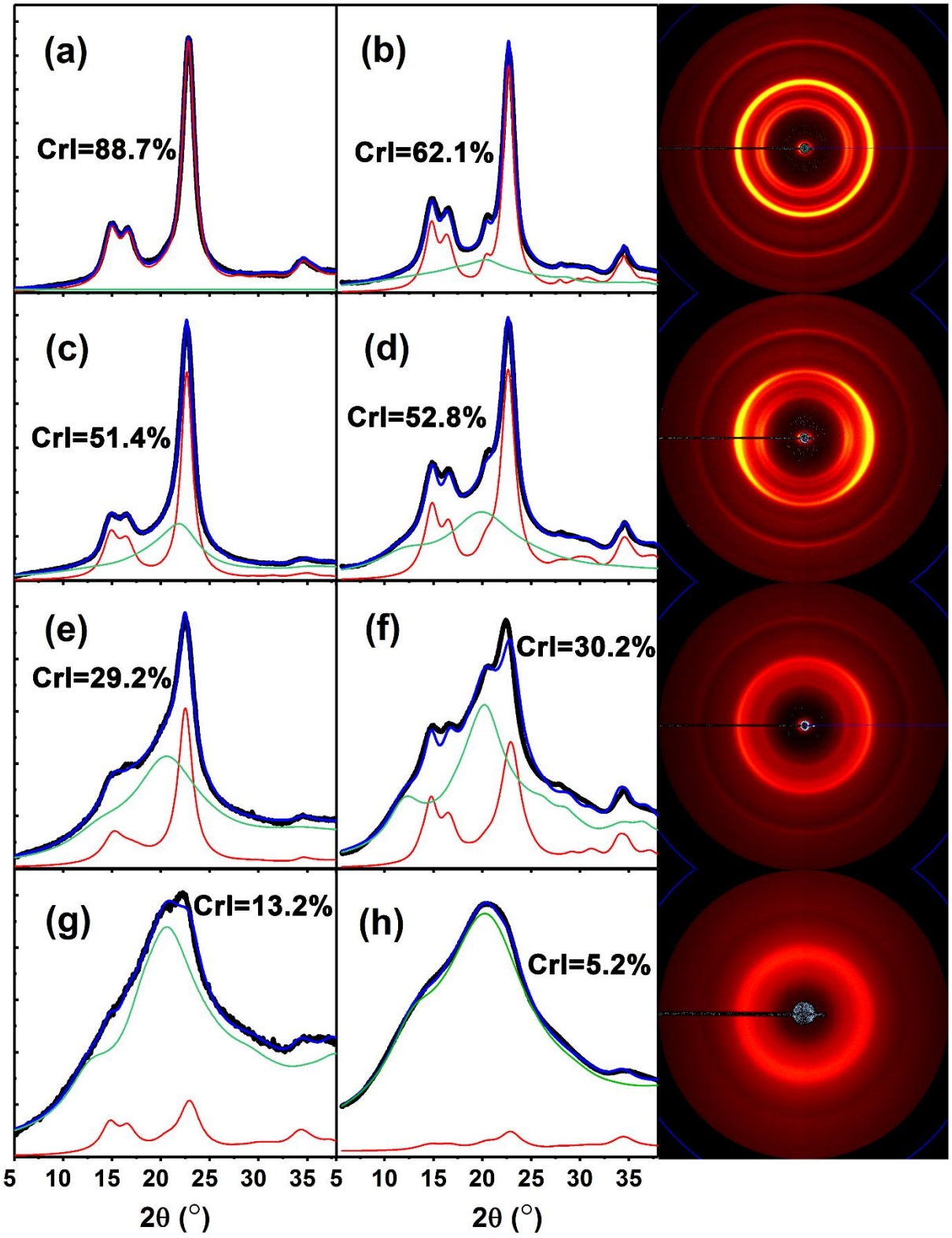
(a)
CrI=88.7%
(b)
CrI=62.1%
(c)
CrI=51.4%
(d)
CrI=52.8%
(e)
CrI=29.2%
(f)
CrI=30.2%
(g)
CrI=13.2%
(h)
CrI=5.2%
5 10 15 20 25 30 35
2θ (°)
5 10 15 20 25 30 35
2θ (°)

730 **Fig. 10** Rietveld refinement analyses of laboratory (a, c, e and g) and synchrotron
731 X-ray results (b, d, f and h) for WMC (a, b), BMC-15 (c, d), BMC-45 (e, f) and
732 BMC-120 (g, h). Black lines are the experimental 1D data; blue, red, and green
733 lines refer to the total fitted line for the analysis, and the modeled crystalline
734 cellulose Iβ and modeled amorphous cellulose contributions, respectively.
735 Backgrounds were experimentally determined and subtracted. The 2D synchrotron
736 X-ray diffraction images related to each sample are plotted to the right of the
737 patterns. The yellow circles or arcs indicate the greatest intensity. Very small gray
738 dots in the beam stop and support areas indicate negative intensity values resulting
739 from background subtraction. They are within the noise levels

740 The crystallite sizes perpendicular to the (200) planes (Fig. 11) were
741 obtained from the fitted cellulose Iβ patterns with the MAUD software. However,
742 the Scherrer equation was applied, rather than MAUD crystallite size values, which
743 are somewhat larger than those calculated with the Scherrer equation. The
744 calculation regions were set at $2\theta=20°$-$25°$, in which the (200) plane of cotton
745 cellulose is included. Both the laboratory and synchrotron X-ray methods showed
746 that the ball-milling treatment not only reduced the fraction of crystalline material
747 but effectively reduces the crystallite sizes (Fig. 11). The trend is in agreement
748 with the decrease of the CrI discussed above but there is better agreement between
749 laboratory and synchrotron results for crystallite size. Diffraction-based

750 determinations of crystallite size are minimum values because the peak widths are
751 affected by the other factors (Huang et al. 2018b).

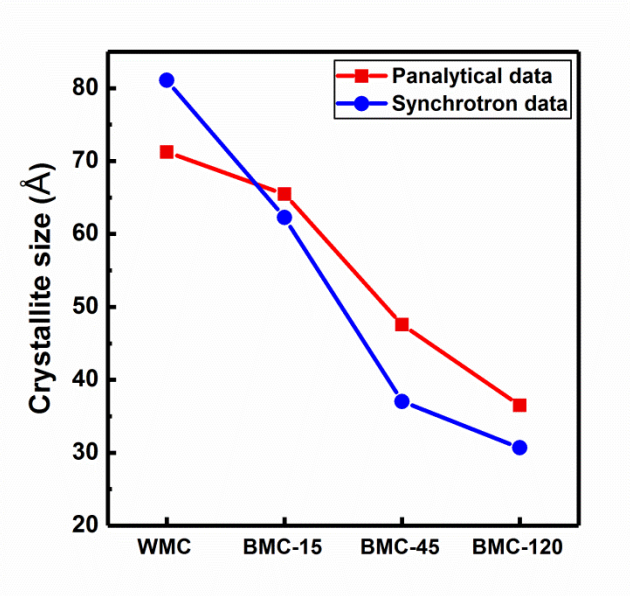

752

753 **Fig. 11** Crystallite sizes perpendicular to the (200) reflections of Wiley milled and
754 ball-milled cotton cellulose determined by laboratory XRD and synchrotron XRD

755

756 The various shapes of the calculated cellulose Iβ and amorphous
757 contributions to the total modeled diffraction intensity have arisen because they are
758 the results of answering the question, "What must be done to the shape of an ideal
759 cellulose diffraction pattern to make it match the experimental one?" Ideally, the
760 individual components would vary in simple ways, such as total number of counts
761 that represent the fraction of total intensity contributed by the component.
762 However, that is not enough variability. The widths of the resolved Iβ component

763 are sharper for the WMC than the BMC, so that must be considered. The
764 laboratory samples clearly have preferred orientation; MAUD can model that
765 component with the March-Dollase equation (Dollase 1986) that changes the
766 intensities of the individual peaks. In the end, to obtain low values of the
767 discrepancy indices (R values), the variations of crystallite size in the different
768 dimensions was also modeled (Popa and Balzar, 2008) that add considerably to the
769 number of variables that were used.
770
771 **Comparison of the methods**
772 A comparison of crystallinity estimates from each of the surveyed methods was
773 undertaken. Although the different analyses in this work measure different
774 properties (Lee et al. 2016b), it is of interest to know how well they agree on the
775 degree of disruption of the structure of the cotton fiber caused by ball milling. In
776 the case of diffraction, we have used a two-phase model that considers both the
777 fraction of amorphous material and the size of the remaining crystalline material.
778 The NMR work indicates the relative fractions of molecules in characteristic
779 environments. Various methods for calculating CrI have been proposed for IR and
780 Raman data, and are employed in this study. SFG-based crystallinity
781 determinations have also been reported, but absent a calibration curve, we assigned
782 a value of a 100% for the CrI of WMC.

783 For the other analyses, we are not aware of existing crystallinity indices
784 based on, for example, carbonyl group increases. Such CrI values would not be
785 widely applicable as there are many reasons that the carbonyl groups could have
786 increased such as intentional oxidation reactions that do not affect crystallinity so
787 much. Still, we felt that it was of interest to derive simple equations that would
788 enable us to compare the crystallinities based on different methods. These
789 relationships are tabulated in Table 2 and plotted in Fig. 12b.
790 Table 2 includes the results from a second, more conventional ^{13}C NMR
791 analysis (Larsson et al. 1999; Massiot et al. 2002) that is fully reported in
792 Supplementary Information. The values of crystallinity in Table 2 for the
793 conventional NMR method were calculated from the sums of the percentages for
794 the four NMR peaks: Iα, I(α+β), Iβ, and the paracrystalline peak (Foston et al.
795 2011; Park et al. 2010). For this conventional method, the ssNMR crystallinity
796 values for the WMC and BMC-15 are very similar, but the BMC-45 and BMC-120
797 results diverge considerably. This result might be partially attributed to water
798 swelling in the conventional ^{13}C NMR samples as part of their preparation. That
799 could lead to some recrystallization or other change in the molecular organization.

800 Every surveyed method for estimating sample crystallinity showed a
801 decrease in value that followed increases in ball-milling time (Table 2, Fig 12).
802 (The pore size measurements, which showed a decrease for BMC-15 and

subsequent increases, were not included.) For example, the WMC samples were more crystalline by any measure than any of their corresponding BMC samples in Fig. 12. Omitting from Fig. 12a the water-soaked conventional ssNMR results and the SFG data, the agreements among the methods is considerably improved. The outlier here is the synchrotron result for WMC. As seen in Fig. 10, the laboratory and synchrotron diffraction patterns differed substantially, most apparently because the laboratory data exhibit preferred orientation of the crystallites. In theory, the results of these two X-ray techniques should agree, and pursuit of the experimental protocols and algorithmic factors in the analysis should improve the inter-method agreement and improve the accuracy of X-ray crystallinity measurements.

816 **Table 2** Comparison of numeric crystallinity values and underlying data

	Laboratory XRD	**Synchrotron XRD**	**ss-NMR**	**ss-NMR[a]**	**FTIR**	**Raman**	**SFG**
Methods	MAUD Rietveld method	MAUD Rietveld method	Cr 88-90ppm Am 80-85ppm	Fitting and modeling of NMR spectra[a]	$CrI=A_{1372\ cm^{-1}}/A_{895cm^{-1}}$	$CrI=[(I_{380\ cm^{-1}}/I_{1096\ cm^{-1}}) -0.0286]/0.0065$	SFG total intensity
Reference	Lutterotti et al. 2007		Kono and Numata 2006	Massiot et al. 2002	Oh et al. 2005	Agarwal et al. 2014	Kim et al. 2015
WMC	88.7%	62.1%	68%	67.5%	72.7%	78.6%	100%
BMC-15	51.4%	52.8%	58%	59.2%	56.9%	56.3%	35%
BMC-45	29.2%	30.2%	28%	45.3%	34.5%	40.4%	9%
BMC-120	13.2%	5.2%	13%	30%	10.7%	13.4%	3%

Samples	**SSA**	**Est CrI**	**DTG**	**Est CrI**	**Carbonyl**	**Est CrI**	**DP (Mn)**	**Est CrI**
WMC	0.8937	87.6%	371.99	95.8%	1.9	88.1%	718	86.3%
BMC-15	1.309	40.8%	369.32	57.9%	15	48%	517	52.8%
BMC-45	1.909	19.2%	367.18	34.3%	21.5	37.5%	344	24%
BMC-120	2.1265	15.4%	362.36	3.7%	36	23.8%	265	10.8%
Estimation Methods	$CrI\ (\%)=70/SSA^2$		$CrI\ (\%)=(DTG-360)^2/1.5$		$CrI\ (\%)=120000/(Carb+35)^2$		$CrI\ (\%)=(DP-200)/6$	

817

818 [a] Conventional SS-NMR method, reported in Supplementary Information

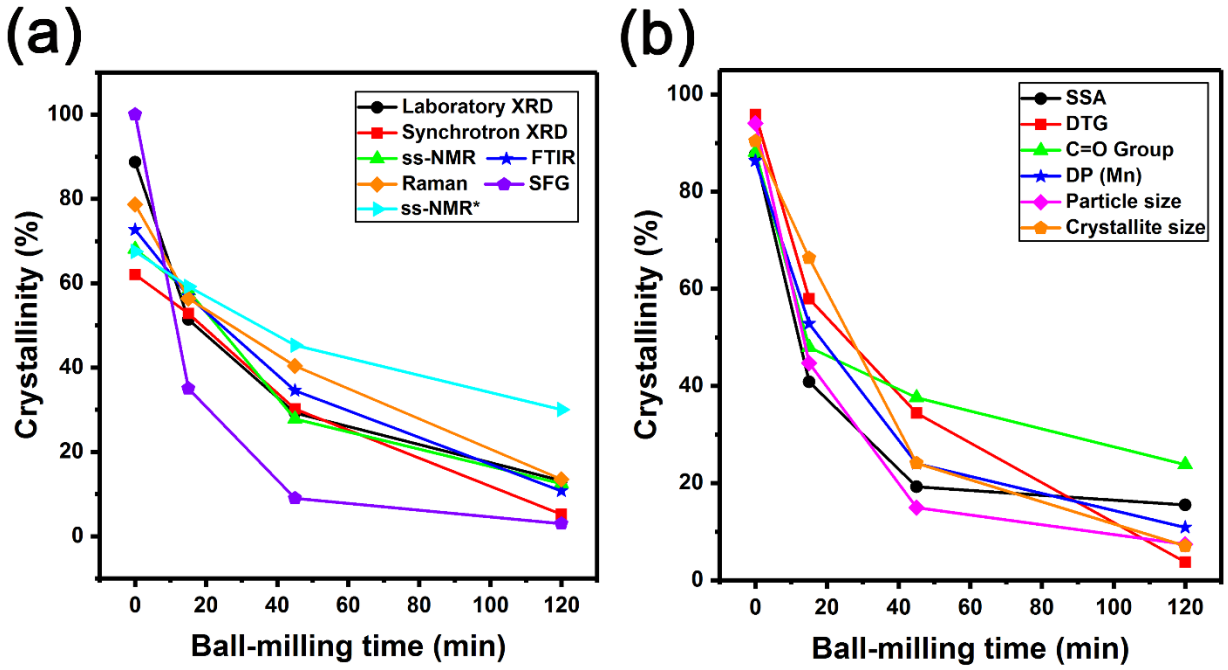

Fig. 12 Plots to compare crystallinity indices from different methods. (a) Those with established relationships. ss-NMR* denotes the conventional NMR analysis (b)Those with proposed relationships from Table 2.

Five different FTIR peak ratios have been proposed to predict crystallinity of cellulose. Those crystallinity values derived from the ratios in Table 3 are plotted in Fig. 13. It seems that the A1372 cm^{-1}/A2900 cm^{-1} ratio and the 1.06 *A1280 cm-^{1} /A1200 cm^{-1} +0.19 equations result in estimates of a too-narrow range of values. Similarly, the Liu et al. method (2012) estimates do not cover enough of the range for the BMC samples. One of the ratios of the Oh et al. studies showed crystallinity values comparable to the other methods reported in Table 2.

Samples	A1372 cm^{-1}/A895 cm^{-1}	A1430 cm^{-1} /A895 cm^{-1}	A1372 cm^{-1}/A2900 cm^{-1}	(1.06*A1280 cm^{-1}/A1200 cm^{-1})+0.19	(A708 cm^{-1}-A800 cm^{-1})/(A730 cm^{-1}-A800 cm^{-1})
WMC	72%	74%	100%	45%	59%
BMC-15	56%	35%	92%	34%	12%
BMC-45	34%	33%	75%	32%	9%
BMC-120	10%	10%	61%	29%	1%
Reference	Oh et al. 2005		Nelson and O'Connor 1964b	Ilharco et al. 1997	Liu et al. 2012

Table 3 Calculations of crystallinity based on FTIR results

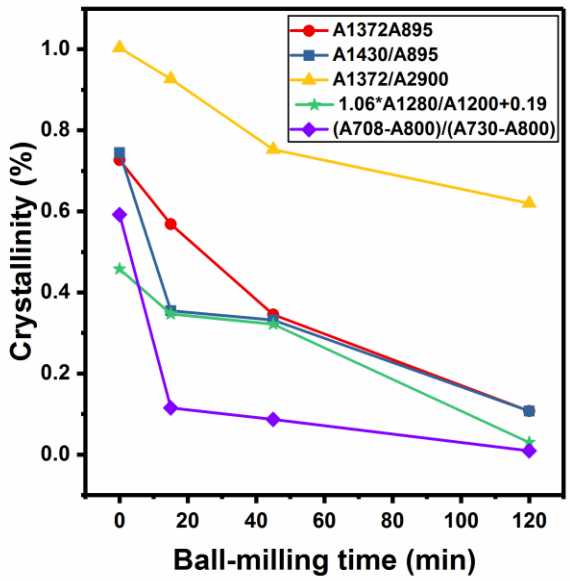

Fig. 13 Comparison of crystallinity indices from various infrared peak ratios (see Table 3)

Conclusions

In this work, cotton cellulose was ball-milled for 15, 45 and 120 min. Multiple approaches concurred that the cellulose crystals were progressively destroyed by the blunt-force impacts of ball milling. The fibers were split open and broken into small bits, the molecular weights decreased, and the cellulose was oxidized on a small scale, as shown by an increase in carbonyl groups. This resulted in more pores and higher surface area of the ball-milled cellulose. There was an increase in water adsorption and a decrease in thermal stability.

According to an average of the two different sets of diffraction experiments, the ball mill reduced the crystalline content of the original cellulose from around 75% to 9%. Ball milling also reduced the crystallite size of the decreasing amount of remaining crystals from about 75 Å to about 35 Å. Except as described below, none of the other results contradicts these basic conclusions.

Results from two other approaches are strongly influenced by neighboring molecules over a range of distances: sum frequency generation vibrational spectroscopy, and ssNMR. They gave reasonable correlations with the X-ray data but the language of the description of decrystallization is different. In the case of SFG, the intensities of the peaks in the OH- and CH- stretch regions decline because of a loss of dipole moment as the sample is decrystallized. In the

858 unmolested crystals of cellulose Iβ, the molecules have parallel packing that results
859 in net dipoles for the crystals. In the case of cellulose II, the individual molecules
860 alternate in packing direction (antiparallel), so there is no net dipole and the SFG
861 spectrum disappears. Somehow, the milling reduces the sizes of the parallel-chain
862 domains, not only by fracturing the parallel-chain crystals of cellulose I, but also
863 by mixing the fragments of adjacent crystallites that have antiparallel orientation
864 (see Introduction), similar to the mercerization treatment but dealing presumably
865 with crystal fragments rather than individual molecules.

866 NMR results, informed by the 2D results in the following paper, gave a
867 surprising result. Namely, there are new molecular structural features created by
868 the ball milling. Although the 1D NMR spectra appeared to experience a general
869 broadening of the peaks as milling progressed (as did the FTIR and Raman
870 spectra), the 2D NMR results could be resolved in terms of peaks that had narrow
871 peak widths. The major ordered component of the 120 minute-ball-milled sample
872 is similar to one of the cellulose Iβ molecules in tunicate cellulose. The major
873 disordered components were most similar to surface molecules of native celluloses
874 that have small crystals (*Arabidopsis, Brachypodium, Zea mays*). Remarkably, the
875 native control cotton did not give peaks with chemical shifts closely similar to
876 those interpreted from the small-crystal plant celluloses. Instead, the control cotton
877 was analyzed in terms of molecular structural species similar to the archetypical

878 *Cladophora* A, A', and tunicate B and B' molecules. In the case of the 120-min
879 ball-milled sample, there were also signals representing four different molecular
880 species. We have not developed any ideas about the domain sizes needed to
881 support the observation of four distinct molecular species by ssNMR in the small
882 (30 Å) remaining crystallites or in the amorphous domains that were modeled with
883 crystals of about 12 Å.

884 Another important finding from the DNP work was that the curve resolution
885 did not depend on a "paracrystalline" component. The more conventional NMR
886 analysis indicated a 27% paracrystalline component for the control cotton, but
887 values of 18.6, 18.9, and 9.7% for the 15-, 45-, and 120-min samples respectively,
888 in complete disagreement with the other analysis. The conventional NMR analysis
889 also reported a large component of inaccessible fibril surface with a very broad
890 width (about 3 ppm). Those values were 15.2, 22.4, 31.5, and 32.5% of the
891 material. There was no need to invoke such a broad peak in the DNP work, nor did
892 the observed increase in BET surface area support the modeled increase of
893 inaccessible surface. Some of the other indicators of crystallinity from FTIR
894 spectroscopy did not perform well enough either.

895 Ball-milled cotton was an interesting sample for analyses of amorphous or
896 non-crystalline cellulose because few other molecules such as hemicellulose or
897 lignin were present. Its initial crystal size is apparently bigger than for many other

plants. Also, all of the samples had the same history until the ball milling began, rather than choosing native materials from different sources to obtain different crystallinities. The choice of cotton balls from Wal-Mart balanced trivial expense and wide availability against a lack of detailed sample history, but they should be similar to other samples of bleached and scoured upland cotton. The diffraction data for the samples is provided in Supplementary Information.

Future efforts could aim to improve the understanding of domain sizes (and size distributions) for the SFG and NMR signals. From the diffraction side, it may be that improvement of the model crystals is necessary to get a better agreement with the observed data. Perhaps more than two crystallite sizes will be needed to reflect a range of crystallite sizes. Also, is it necessary to employ the random quarter-up or quarter-down shifting of molecules described by Driemeier and Francisco (2014)? How do structures of crystals in the common plants with smaller crystals differ from being smaller pieces of tunicate crystals?

Acknowledgments

The authors gratefully acknowledged the support by Chinese Scholarship Council (CSC No.201706510045) for ZL. The NMR work was supported by National Science Foundation (NSF OIA-1833040). The SFG work was supported by the Center for Lignocellulose Structure and Formation, Energy Frontier Research

Center funded by the U.S. Department of Energy, Office of Science, Basic Energy Sciences, under Award Number DE-SC0001090. Prof. Nathaniel C. Gilbert at CAMD kindly helped with the synchrotron X-ray diffraction analysis, and Dr. Dongmei Cao at the Louisiana State University Shared Instrument Facility provided the FE-SEM micrographs. Stephanie Beck of FPInnovations and Hee Jin Kim of the Southern Regional Research Center reviewed the manuscript. Acknowledgements are also made to Catrina Ford for technical assistance.
Mention of trade names or commercial products in this publication is solely for the purpose of providing specific information and does not imply recommendation or endorsement by the U.S. Department of Agriculture. USDA is an equal opportunity provider and employer.

References

Agarwal UP, Ralph SA (1997) FT-Raman spectroscopy of wood: Identifying contributions of lignin and carbohydrate polymers in the spectrum of black spruce (*Picea mariana*). Appl Spectrosc 51:1648–1655. doi: 10.1366/0003702971939316

Agarwal UP (2014) 1064 nm FT-Raman spectroscopy for investigations of plant cell walls and other biomass materials. Front Plant Sci 5: 490

938 Agarwal UP, Ralph SA, Reiner RS, Baez C (2016) Probing crystallinity of never-
939 dried wood cellulose with Raman spectroscopy. Cellulose 23:125–144. doi:
940 10.1007/s10570-015-0788-7
941 Ahvenainen P, Kontro I, Svedström (2016) Comparison of sample crystallinity
942 determination methods by X-ray diffraction for challenging cellulose I
943 materials. Cellulose 23:1073–1086
944 Atalla RH, Gast JC, Sindorf, DW, Bartuska VJ, Maciel GE (1980) Carbon-13
945 NMR spectra of cellulose polymorphs. J Am Chem Soc 102(9): 3249–3251
946 Atalla RH, Vanderhart DL (1984) Native cellulose: A composite of two distinctive
947 crystalline forms. Science 223: 283–285
948 Barnette AL, Bradley LC, Veres BD, Schreiner EP, Park J, Park S, Kim SH (2011)
949 Selective detection of crystalline cellulose in plant cell walls with sum
950 frequency generation (SFG) vibration spectroscopy. Biomacromolecules
951 12:2434–2439
952 Barnette AL, Lee C, Bradley LC, Schreiner EP, Park H, Shin H, Cosgrove DJ,
953 Park S, Kim SH (2012) Quantification of crystalline cellulose in
954 lignocellulosic biomass using sum frequency generation (SFG) vibration
955 spectroscopy and comparison with other analytical methods" Carbohydr
956 Polym 89:802–809
957 Bertran MS, Dale BE (1986) Determination of cellulose accessibility by

958 differential scanning calorimetry. J Appl Polym Sci 32:4241–4253
959 Brunauer S, Emmett PH, Teller E (1938) Adsorption of gases in multimolecular
960 layers. J Am Chem Soc 60:309–319
961 Chen L, Wang Q, Hirth K, Baez C, Agarwal UP,Zhu JY (2015) Tailoring the yield
962 and characteristics of wood cellulose nanocrystals (CNC) using concentrated
963 acid hydrolysis. Cellulose 22:1753–1762
964 Dollase WA (1986) Correction of intensities for preferred orientation in powder
965 diffractometry: application of the March model. J Appl Crystallogr 19(4):267–
966 272.
967 Driemeier C, Calligaris GA (2011) Theoretical and experimental developments for
968 accurate determination of crystallinity of cellulose I materials. J Appl Cryst
969 44:184–192
970 Driemeier C (2014) Two-dimensional Rietveld analysis of celluloses from higher
971 plants. Cellulose 21:1065–1073
972 Driemeier C, Francisco LH (2014) X-ray diffraction from faulted cellulose I
973 constructed with mixed Iα–Iβ stacking. Cellulose 21:3161–3169
974 Duchemin B (2017) Size, shape, orientation and crystallinity of cellulose Iβ by X-
975 ray powder diffraction using a free spreadsheet program. Cellulose 24:2727–
976 2741
977 Forziati FH, Stone WK, Rowen JW, Appel WD (1950) Cotton powder for infrared

transmission measurements. J Res Nat Bur Stand 45: 109–113

Foston MB, Hubbell CA, Ragauskas AJ (2011) Cellulose Isolation Methodology for NMR Analysis of Cellulose Ultrastructure. Materials 4:1985–2002

French AD (2014) Idealized powder diffraction patterns for cellulose polymorphs. Cellulose 21:885–896. DOI: 10.1007/s10570-013-0030-4

French AD, Santiago Cintrón M (2013) Cellulose polymorphy, crystallite size, and the Segal crystallinity index. Cellulose 20:583–588

French AD, Pérez S, Bulone V, Rosenau T, Gray D (2018) Cellulose, in Encyclopedia of Polymer Science and Technology DOI: 10.1002/0471440264.pst042.pub2

French AD, Kim HJ (2018) Cotton fiber structure, in Fang D ed. Cotton fiber, physics and biology DOI: 10.1007/978-3-030-00871-0_2

Harris DM, Corbin K, Wang T, Gutierrez R, Bertolo AL, Petti C, Smilgies D-M, Estevez JM, Bonetta D, Urbanowicz BR, Ehrhardt DW, Somerville CR, Rose JKC, Hong M, Debolt S (2012) Cellulose microfibril crystallinity is reduced by mutating C-terminal transmembrane region residues CESA1^{A903V} and CESA3^{T942I} of cellulose synthase. Proc Natl Acad Sci 109:4098–4103

Hearle JWS (1958) A fringed fibril theory of structure in crystalline polymers. J Polym Sci 28:432–435

Holzwarth U, Gibson N (2011) The Scherrer equation versus the'Debye-Scherrer

998 equation'. Nat Nanotechnol 6:534
999 Howell C, Hastrup ACS, Jara R, Larsen FH, Goodell B, Jellison J (2011) Effects of
1000 hot water extraction and fungal decay on wood crystalline cellulose structure.
1001 Cellulose 18:1179–1190
1002 Huang S, Makarem M, Kiemle SN, Hamedi H, Sau M, Cosgrove DJ, Kim SH
1003 (2018a) Inhomogeneity of cellulose microfibril assembly in plant cell walls
1004 revealed with sum frequency generation microscopy. J Phys Chem B
1005 122:5006–5019
1006 Huang S, Makarem M, Kiemle SN, Zheng Y, Xin H, Ye D, Gomez EW, Gomez
1007 ED, Cosgrove DJ, Kim SH (2018b) Investigating dehydration-induced
1008 physical strains of cellulose microfibrils in plant cell walls. Carbohydr Polym
1009 197:337–348
1010 Ilharco LM, Garcia AR, Silva JL, Ferreira FV (1997) Infrared Approach to the S
1011 tudy of Adsorption on Cellulose: Influence of Cellulose Crystallinity on the
1012 Adsorption of Benzophenone. Langmuir 13(15): 4126-4132.
1013 Isogai A, Atalla RH (1991) Amorphous celluloses stable in aqueous media:
1014 Regeneration from SO2–amine solvent systems. J Polym Sci Part A Polym
1015 Chem 29:113–119
1016 Kirui A, Ling Z, Kang X, Dickwella Widanage MC, Mentink—Vigier F, French
1017 AD, Wang T (2019) Atomic resolution of cotton cellulose structure enabled by

Dynamic Nuclear Polarization Solid-State NMR. Cellulose 26:XXXX–XXYY

Klug HP, Alexander LE (1974) X-ray diffraction procedures: for polycrystalline and amorphous materials. X-Ray Diffr Proced Polycryst Amorph Mater 2nd Ed. Klug HP, Alexander LE Eds., pp 992 ISBN 0-471-49369-4 Wiley-VCH

Kono H, Numata Y (2006) Structural investigation of cellulose I α and I β by 2D RFDR NMR spectroscopy: determination of sequence of magnetically inequivalent D-glucose units along cellulose chain. Cellulose 13:317–326

Langan P, Nishiyama Y, Chanzy H (2001) X-ray structure of mercerized cellulose II at 1 Å resolution. Biomacromolecules 2:410–416

Larsson PT, Hult EL, Wickholm K, Pettersson E, Iversen T (1999) CP/MAS ^{13}C NMR spectroscopy applied to structure and interaction studies on cellulose I. Solid State Nucl Magn Reson 15:31-40

Lee CM, Mohamed NMA, Watts HD, Kubicki JD, Kim SH (2013) Sum-frequency-generation vibration spectroscopy and density functional theory calculations with dispersion corrections (DFT-D2) for cellulose Iα and Iβ. J Phys Chem B 117:6681–6692

Lee C, Kafle K, Park Y-B, Kim SH (2014) Probing crystal structure and mesoscale assembly of cellulose microfibrils in plant cell walls, tunicate tests, and bacterial films using vibrational sum frequency generation (SFG) spectroscopy" Phys Chem Chem Phys 16:10844–10853

1038 Lee CM, Kafle K, Huang S, Kim SH (2015a) Multimodal broadband vibrational
1039 sum frequency generation (MM-BB-V-SFG) spectrometer and microscope. J
1040 Phys Chem B 120:102–116
1041 Lee CM, Kubicki JD, Xin B, Zhong L, Jarvis MC, Kim SH (2015b) Hydrogen
1042 bonding network and OH stretch vibration of cellulose: Comparison of
1043 computational modeling with polarized IR and SFG spectra. J Phys Chem B
1044 119:15138–15149
1045 Lee CM, Chen X, Weiss PA, Jensen L, Kim SH (2016a) Quantum mechanical
1046 calculations of vibrational sum-frequency-generation (SFG) spectra of
1047 cellulose: dependence of the ch and oh peak intensity on the polarity of
1048 cellulose chains within the SFG coherence domain. J Phys Chem Lett 8:55–60
1049 Lee CM, Dazen K, Kafle K, Moore A, Johnson DK, Park S, Kim SH (2016b)
1050 Correlations of apparent cellulose crystallinity characterized by estimated from
1051 different characterization techniques: XRD, NMR, IR, Raman, & and SFG.
1052 Adv Polym Sci 271:115–131
1053
1054 Liu Y, Thibodeaux D, Gamble G, Bauer P, VanDerveer D (2012) Comparative
1055 investigation of Fourier transform infrared (FT-IR) spectroscopy and X-ray
1056 diffraction (XRD) in the determination of cotton fiber crystallinity. Appl
1057 Spectrosc 66:983–986

1058 Liu Y, Kim HJ (2015) Use of attenuated total reflection fourier transform infrared
1059 (ATR FT-IR) Spectroscopy in direct, nondestructive, and rapid assessment of
1060 developmental cotton fibers grown in planta and in culture. Appl Spectrosc
1061 69:1004–1010
1062 Lutterotti L, Bortolotti M, Ischia G, Lonardelli I, Wenk H-R, (2007) Rietveld
1063 texture analysis from diffraction images, Z Kristallogr, Suppl. 26, 125–130
1064 Makarem M, Lee CM, Sawada D, O'Neill HM, Kim SH (2017) Distinguishing
1065 surface versus bulk hydroxyl groups of cellulose nanocrystals using vibrational
1066 sum frequency generation spectroscopy. J Phys Chem Letts 9:70–75
1067 Makarem M, Lee CM, Kafle K, Huang S, Chae I, Yang H, Kubicki JD, Kim SH
1068 (2019) Probing cellulose structures with vibrational spectroscopy. Cellulose
1069 26:XXXX-XXYY
1070 Massiot D, Fayon F, Capron M, King I, Le Calvé S, Alonso B, Durand J-O, Bujoli
1071 B, Gan Z, Hoatson G (2002) Modelling one- and two- dimensional solid-
1072 state NMR spectra. Magn Reson Chem 40:70–76
1073 Millett MA, Effland MJ, Caulfield DF (1979) Influence of fine grinding on the
1074 hydrolysis of cellulosic materials-acid vs. enzymatic. Adv Chem Ser 181:71–
1075 89
1076 Nelson ML, O'Connor RT (1964a) Relation of certain infrared bands to cellulose
1077 crystallinity and crystal lattice type. Part II. A new infrared ratio for estimation

of crystallinity in celluloses I and II. J Appl Polym Sci 8:1325–1341. doi: 10.1002/app.1964.070080323

Nelson ML, O'Connor RT (1964b) Relation of certain infrared bands to cellulose crystallinity and crystal latticed type. Part I. Spectra of lattice types I, II, III and of amorphous cellulose. J Appl Polym Sci 8:1311–1324

Newman RH, Hemmingson JA (1990) Determination of the degree of cellulose crystallinity in wood by carbon-13 Nuclear Magnetic Resonance Spectroscopy. Holzforschung 44:351–356

Newman RH, Hill SJ, Harris PJ (2013) Wide-angle X-ray scattering and solid-state nuclear magnetic resonance data combined to test models for cellulose microfibrils in mung bean cell walls. Am Soc Plant Biol 163:1558–1567

Nishiyama Y, Langan P, Chanzy H (2002) Crystal structure and hydrogen-bonding system in cellulose Iβ from synchrotron X-ray and neutron fiber diffraction. J Am Chem Soc 124:9074–9082

Nishiyama Y, Sugiyama J, Chanzy H, Langan P (2003a) Crystal structure and hydrogen bonding system in cellulose Iα from synchrotron x-ray and neutron fiber diffraction. J Am Chem Soc 125:14300–14306. doi: ja0257319

Nishiyama Y, Kim U-J, Kim D-Y, Katsumata KS, May RP, and Langan P (2003b) Periodic disorder along ramie cellulose microfibrils. Biomacromolecules 4:1013–1017

1098 Oh SY, Yoo D, Shin Y, Kim HC, Kim HY et al (2005) Crystalline structure
1099 analysis of cellulose treated with sodium hydroxide and carbon dioxide by
1100 means of X-ray diffraction and FTIR spectroscopy. Carbohyd. Res. 340: 2376-
1101 2391.
1102 Park S, Baker JO, Himmel ME, Parrilla PA, Johnson DK (2010) Cellulose
1103 crystallinity index: measurement techniques and their impact on interpreting
1104 cellulase performance. Biotechnol Biofuels 3:10
1105 Park YB, Lee CM, Koo B-W, Park S, Cosgrove DJ, Kim SH (2013) Monitoring
1106 meso-scale ordering of cellulose in intact plant cell walls using sum frequency
1107 generation (SFG) spectroscopy. Plant Physiol 163:907–913
1108 Phyo P, Wang T, Yang Y, O'Neill H, Hong M (2018) Direct determination of
1109 hydroxymethyl conformations of plant cell wall cellulose using ^{1}H polarization
1110 transfer solid-state NMR. Biomacromolecules 19:1485–1497
1111 Popa NC, Balzar D (2008) Size-broadening anisotropy in whole powder pattern
1112 fitting. J Appl Cryst 41:615–627
1113 Application to zinc oxide and interpretation of the apparent
1114 crystallites in terms of physical models
1115 Reyes DCA, Skoglund N, Svedberg A, Eliasson B, Sundman O (2016) The
1116 influence of different parameters on the mercerisation of cellulose for viscose
1117 production. Cellulose 23:1061–1072

Rietveld H (1969) A profile refinement method for nuclear and magnetic structures. J Appl Crystallogr 2:65–71

Rodriguez-Navarro AB (2006) XRD2DScan: new software for polycrystalline materials characterization using two-dimensional X-ray diffraction. J Appl Crystallogr 39:905–909

Röhrling J, Potthast A, Rosenau T, Lange T, Borgards A, Sixta H, Kosma P (2002) A novel method for the determination of carbonyl groups in cellulosics by fluorescence labeling. 2. Validation and applications. Biomacromolecules 3: 969–975

Rollin JA, Zhu Z, Sathitsuksanoh N, Zhang YP (2011) Increasing cellulose accessibility is more important than removing lignin: A comparison of cellulose solvent- based lignocellulose fractionation and soaking in aqueous ammonia. Biotechnol Bioeng 108:22–30

Sarko A, Nishimura H, Okano T (1987) Crystalline alkali-celllulose complexes as intermediates during mercerization. ACS Symp Ser 340:169–177

Schenzel K, Fischer S, Brendler E (2005) New method for determining the degree of cellulose I crystallinity by means of FT Raman spectroscopy. Cellulose 12:223–231. doi: 10.1007/s10570-004-3885-6

Schroeder LR, Gentile VM, Atalla RH (1986) Nondegradative preparation of amorphous cellulose. J Wood Chem Technol 6:1–14

Segal L, Creely JJ, Martin a. E, Conrad CM (1959) An empirical method for estimating the degree of crystallinity of native cellulose using the X-Ray diffractometer. Text Res J 29:786–794. doi: 10.1177/004051755902901003

Sehaqui H, Zhou Q, Berglund LA (2011) High-porosity aerogels of high specific surface area prepared from nanofibrillated cellulose (NFC). Compos Sci Technol 71:1593–1599

Shibazaki H, Kuga S, Okano T (1997) Mercerization and acid hydrolysis of bacterial cellulose. Cellulose 4:75–87

Sugiyama J, Persson J, Chanzy H (1991) Combined infrared and electron diffraction study of the polymorphism of native celluloses. Macromolecules 24:2461–2466

Takahashi H, Lee D, Dubois L, Bardet M, Hediger S, De Paëpe G (2012) Rapid natural- abundance 2D ^{13}C–^{13}C correlation spectroscopy using Dynamic Nuclear Polarization Enhanced Solid- State NMR and matrix- free sample preparation. Angew Chemie Int Ed 51:11766–11769

Thygesen A, Oddershede J, Lilholt H, Thomsen AB, Ståhl (2005) On the determination of crystallinity and cellulose content in plant fibres. Cellulose 12:563–576

Vanderfleet OM, Reid MS, Bras J, Heux L, Godoy-Vargas J, Panga MKR, Cranston ED (2019) Insight into thermal stability of cellulose nanocrystals

from new hydrolysis methods with acid blends. Cellulose 26:XXX–XXX (This issue)

Viëtor RJ, Newman RH, Ha MA, Apperley DC, Jarvis MC (2002) Conformational features of crystal-surface cellulose from higher plants. Plant J 30(6) 721–731

Wang T, Hong M (2016) Solid-state NMR investigations of cellulose structure and interactions with matrix polysaccharides in plant primary cell walls. J Exp Bot 67: 503–514

Wertz J-L, Mercier JP, Bédué O (2010) Cellulose sciense and technology. Taylor& Francis Group

Wickholm K, Larsson PT, Iversen T (1998) Assignment of non-crystalline forms in cellulose I by CP/MAS ^{13}C NMR spectroscopy. Carbohydr Res 312:123–129

Wiley JH, Atalla RH (1987) Band assignments in the Raman spectra of celluloses. Carbohydr Res 160:113–129

Xiaohui J, Bowden M, Brown EE, Zhang X (2015) An improved X-ray diffraction method for cellulose crystallinity measurement. Carbohydr Polym 123:476–481

Yang H, Wang T, Oehme D, Petridis L, Hong M, Kubicki JD (2018) Structural factors affecting ^{13}C NMR chemical shifts of cellulose: a computational study. Cellulose 25:23–36

Young RA ed. (1993) The Rietveld Method. IUCr Monographs in Crystallography. 5. International Union of Crystallography, Oxford University Press, New York, NY. pp. 298